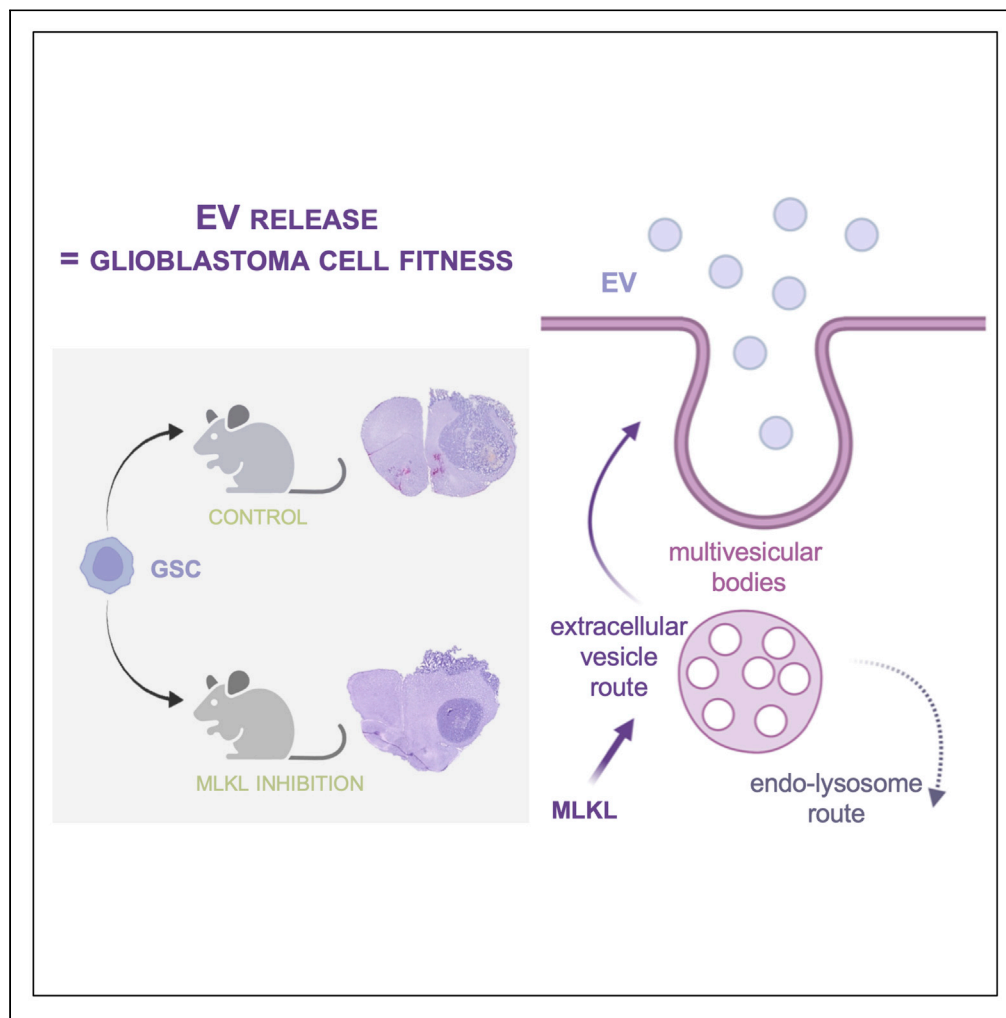


Article

Inhibition of the pseudokinase MLKL alters extracellular vesicle release and reduces tumor growth in glioblastoma



Gwennan André-Grégoire, Clément Maghe, Tiphaine Douanne, ..., Jacky G. Goetz, Nicolas Bidère, Julie Gavard

julie.gavard@inserm.fr

Highlights

The pseudokinase MLKL governs extracellular vesicle release in glioblastoma cells

Blocking MLKL is deleterious to glioblastoma cell expansion *in vitro* and *in vivo*

MLKL action in glioblastoma patient cells does not involve necroptosis death

MLKL inhibition potentiates TMZ-induced cell death in glioblastoma patient cells

André-Grégoire et al.,
iScience 25, 105118
October 21, 2022 © 2022 The Author(s).
<https://doi.org/10.1016/j.isci.2022.105118>

Article

Inhibition of the pseudokinase MLKL alters extracellular vesicle release and reduces tumor growth in glioblastoma

Gwennan André-Grégoire,^{1,2,3} Clément Maghe,^{1,3} Tiphaine Douanne,^{1,3} Sara Rosińska,^{1,3} Fiorella Spinelli,^{1,3} An Thys,^{1,3} Kilian Trillet,^{1,3} Kathryn A. Jacobs,^{1,3} Cyndie Ballu,^{1,3} Aurélien Dupont,⁴ Anne-Marie Lyne,^{5,6,7} Florence M.G. Cavalli,^{5,6,7} Ignacio Busnelli,^{3,8} Vincent Hyenne,^{3,8,9} Jacky G. Goetz,^{3,8,9} Nicolas Bidère,^{1,3} and Julie Gavard^{1,2,3,10,*}

SUMMARY

Extracellular vesicles (EVs) are lipid-based nanosized particles that convey biological material from donor to recipient cells. EVs play key roles in glioblastoma progression because glioblastoma stem-like cells (GSCs) release pro-oncogenic, pro-angiogenic, and pro-inflammatory EVs. However, the molecular basis of EV release remains poorly understood. Here, we report the identification of the pseudokinase MLKL, a crucial effector of cell death by necroptosis, as a regulator of the constitutive secretion of EVs in GSCs. We find that genetic, protein, and pharmacological targeting of MLKL alters intracellular trafficking and EV release, and reduces GSC expansion. Nevertheless, this function ascribed to MLKL appears independent of its role during necroptosis. *In vivo*, pharmacological inhibition of MLKL reduces the tumor burden and the level of plasmatic EVs. This work highlights the necroptosis-independent role of MLKL in vesicle release and suggests that interfering with EVs is a promising therapeutic option to sensitize glioblastoma cells.

INTRODUCTION

Glioblastoma (GBM) is the most prevalent and aggressive primary brain tumor in adults. This cancer remains mostly incurable because the median survival is estimated at 14 months (Stupp et al., 2005). Established in 2005 (Stupp et al., 2005), the therapeutic regimen encompasses resective surgery, followed by concomitant radio-chemotherapy using the alkylating agent temozolomide (TMZ). Relapse is rapid and fatal, with scarce, palliative second-line treatment options. Thus, optimized therapies are urgently needed. GBM aggressiveness partially relies on a subpopulation of highly plastic, malignant cells with stem properties named GSCs (for Glioblastoma Stem-like Cells) that may act as a reservoir able to repeatedly initiate and repopulate the tumor mass (Gimple et al., 2019). GSCs also resist radio and chemotherapy (André-Grégoire et al., 2018; Bao et al., 2006; Chen et al., 2012) and pervert the tumor microenvironment to support their maintenance, growth, and expansion.

Extracellular vesicles (EVs) are important mediators of cell-to-cell communication within the tumor soil (André-Grégoire and Gavard, 2017; Quezada et al., 2018). EVs are lipid-bilayer carriers, typically emanating from either the intracellular endosomal compartment (exosomes) or budding at the plasma membrane (microvesicles). These nano-sized particles ranging from 30–100 nm to a few micrometers haul proteins, lipids, and nucleic acids (van Niel et al., 2018). EVs are suspected to support cancer growth and dissemination by mediating both local and at-distance signaling (André-Grégoire and Gavard, 2017; Gao et al., 2020). For example, GBM-derived EVs circulate in biofluids and transfer oncogenic material, such as the EGFRvIII variant (Al-Nedawi et al., 2008) or the active oncogene Ras (Luhtala et al., 2017), to neighboring non-tumor cells. Tumor EVs also assist in endothelial defects and angiogenesis. Indeed, the uptake by endothelial cells of tumor EVs enriched with pro-angiogenic factors, results in the formation of tubules (Skog et al., 2008) and the loss of vascular barrier integrity (Treps et al., 2016, 2017). Likewise, EVs contribute to cell proliferation and tumor growth (Skog et al., 2008), and can induce immunotolerance (Harshyne et al., 2016; deVrij et al., 2015). Alongside this role on the tumor stroma, EVs participate in

¹Team SOAP, CRCI2NA, Nantes Université, Inserm, CNRS, Université d'Angers, Nantes, France

²Institut de Cancérologie de l'Ouest (ICO), Saint-Herblain, France

³Equipe Labellisée Ligue Contre le Cancer, Paris, France

⁴SFR UMS CNRS 3480, INSERM 018, Biosit Biologie, Santé, Innovation Technologique, Rennes, France

⁵Institut Curie, PSL Research University, Paris, France

⁶Inserm, U900, Paris, France

⁷MINES ParisTech, CBIO - Centre for Computational Biology, PSL Research University, Paris, France

⁸INSERM UMR_S1109, Tumor Biomechanics, Université de Strasbourg, Fédération de Médecine Translationnelle de Strasbourg (FMTS), Strasbourg, France

⁹CNRS SNC5055, Strasbourg, France

¹⁰Lead contact

*Correspondence:

Julie.gavard@inserm.fr

<https://doi.org/10.1016/j.isci.2022.105118>



GBM aggressiveness and resistance to treatments. For instance, chemotherapy with TMZ impacts the number and content of EV-transported ribonucleic acids and proteins, which in turn convey TMZ resistance (Garnier et al., 2018; Yin et al., 2019; Zeng et al., 2018; Zhang et al., 2019). In this context, GSCs cope with TMZ toxic signals, shifting their EV protein cargoes towards a cell adhesion signature (André-Grégoire et al., 2018).

Although virtually every cell type might empower the intracellular machinery to release EVs on diverse stimuli (van Niel et al., 2018), cancer cells constitutively hijack this cell-to-cell communication route to dispatch mutations, metabolic changes, and resistance to treatments (Skog et al., 2008). However, the detailed molecular mechanisms involved in tumor EV biogenesis and their further impact on disease progression remain unclear. In the search for mediators of EV release in GBM, clinical data mining identified the mixed lineage kinase domain-like protein, MLKL. This pseudokinase is a key effector of cell death by necroptosis, a regulated form of necrosis that occurs in apoptosis-deficient conditions (Sun et al., 2012; Zhao et al., 2012). MLKL also exerts non-necroptotic functions, such as controlling adhesion molecule expression in endothelial cells (Dai et al., 2020), regeneration after nerve injury (Ying et al., 2018), endosomal compartment trafficking and constitutive release of EVs, as well as necroptosis-associated vesicle formation and extrusion (Douanne et al., 2019; Gong et al., 2017; Shlomovitz et al., 2021; Yoon et al., 2017; Zargarian et al., 2017). MLKL, therefore, operates dual functions at the crossroads between life-death checkpoints and intercellular communication within the tumor microenvironment. By deploying a triad of complementary interfering approaches (siRNA, drug, and targeted acute protein degradation), we demonstrate that blocking MLKL modifies the release of EVs and slows down the expansion of patient-derived GSCs *in vitro* and *in vivo*.

RESULTS

Aggressive glioblastoma cells express MLKL

To identify EV-related genes whose expression might impact the disease outcome, we interrogated The Cancer Genome Atlas (TCGA) online database through the Gliovis platform (Bowman et al., 2017). The analysis of 69 genes related to EV production (van Niel et al., 2018) and segregated between high and low levels of RNA expression identified 9 candidates, which were significantly associated with the probability of survival in GBM patients (Figure 1A). In addition to the instrumental regulator of EV production RAB27A (Ostrowski et al., 2010), we found that the expression level of SYTL3 and MLKL were inversely correlated with GBM patient survival (Figure 1B). Besides its key function in orchestrating cell death via necroptosis (Sun et al., 2012; Zhao et al., 2012), MLKL was reported to play an important role in endosomal trafficking and EV biogenesis (Gong et al., 2017; Yoon et al., 2017). Alongside its prognosis value in survival probability, MLKL mRNA expression was heightened in GBM, as compared to non-tumor brains (Figures 1C and 1D). Of note, the level of MLKL mRNA is augmented according to the tumor grade (Figure 1C). Likewise, MLKL expression is lower in patients with an isocitrate dehydrogenase (*IDH*)-1 gene somatic mutation, typically associated with a younger age at diagnosis, and a better prognosis (Yan et al., 2009) (Figure 1C). Of interest, MLKL expression was observed across the four reported Verhaak molecular subtypes, with higher levels in the mesenchymal (MES) tumors (Verhaak et al., 2010) (Figure 1C). mRNA level of MLKL was also associated with worsened survival prognosis (Figure 1D). This elevated expression was further confirmed at the protein level in brain biopsies (Figure 1E).

Although curated database analyses indicate that MLKL expression is typically associated with the myeloid compartment in the brain (The Human Protein Atlas, <https://www.proteinatlas.org/>; Karlsson et al., 2021), less is known concerning patient-derived GSCs, a population of cells exhibiting stem-like properties thought to be responsible for the initiation, maintenance, and recurrence of the tumor (Harford-Wright et al., 2017; Singh et al., 2004). We found that the MLKL protein is readily detectable in GSCs from several patients (Figure 1F). Of interest, the abundance of MLKL was concomitantly reduced at the RNA and protein levels in Differentiated Glioblastoma Stem-like Cells (DGCs, Figure S1) (André-Grégoire et al., 2018). Morphological differentiation (Figure S1A), reduction in the expression of the SOX2 stem marker, and increase in the expression of the TUBB3 neural differentiation marker (Figures S1B and S1C) confirmed the differentiation status of the sister DGCs. Altogether, our data support the notion that MLKL expression is associated with aggressiveness in glioma clinical samples. Although it cannot be excluded that this is at least in part because of MLKL expression in myeloid cells, there is detectable expression in patient-derived tumor cells, and MLKL might notably be related to the stem-like cellular population.

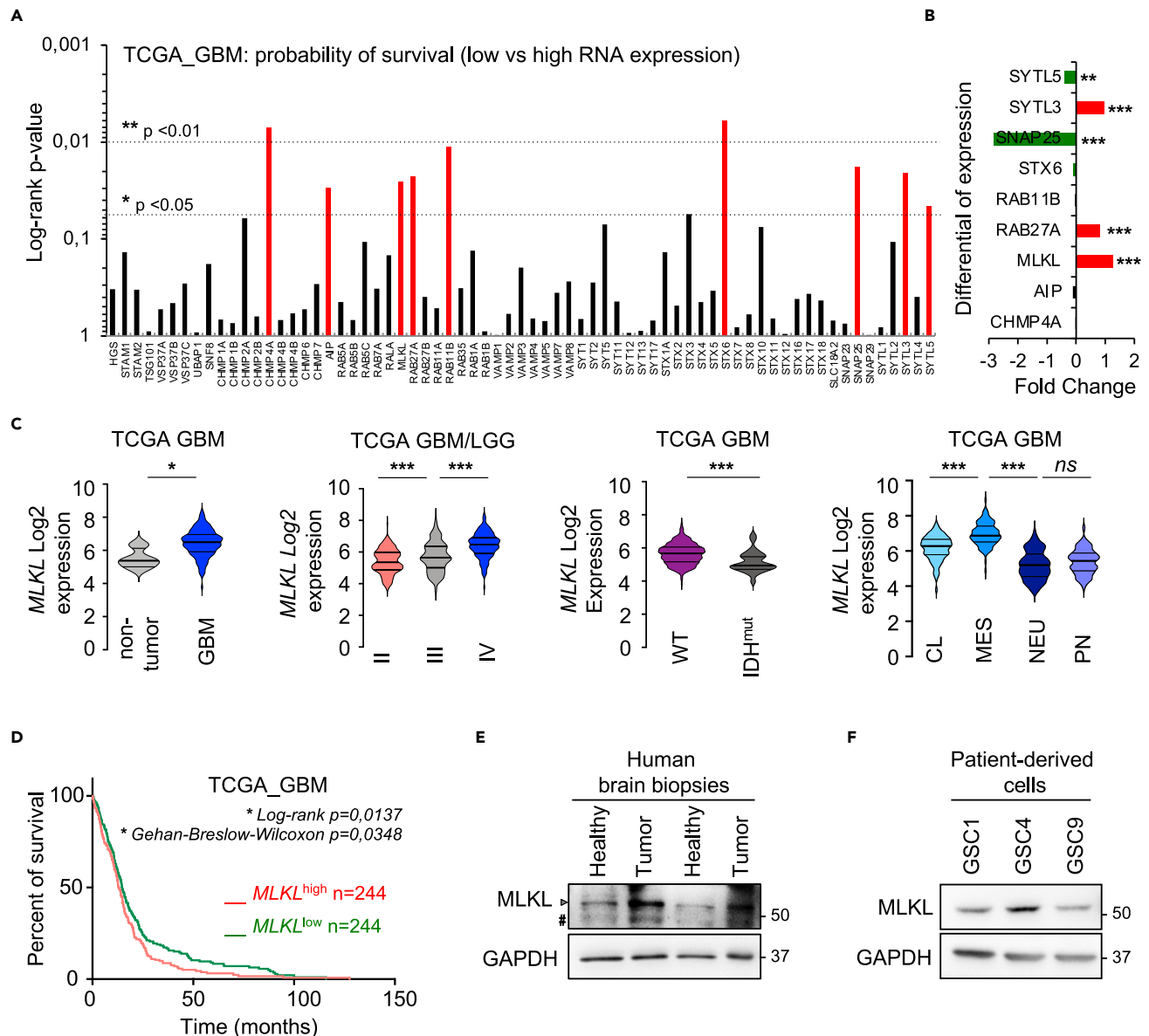


Figure 1. The expression of the pseudokinase MLKL is associated with aggressive glioma

(A) The Cancer Genome Atlas (TCGA RNAseq dataset) was interrogated via the Gliovis platform to analyze the probability of survival (log-rank p-value) in 156 GBM patients, stratified based on low vs high expression (median cut-off) of 69 EV-related genes. Probability of survival was significantly changed for nine of them (namely SYTL5, SYTL3, SNAP25, STX6, RAB11B, RAB27A, MLKL, AIP, and CHMP4A).

(B) Fold changes in mRNA expression for the 9 genes selected from panel (a) in non-tumor vs GBM patients.

(C) Box plots of MLKL mRNA expression in non-tumor, low-grade glioma (LGG grades II and III), and in GBM (grade IV), according to the mutation status of IDH1 (IDH1^{mut}) and the GBM subtypes (classical CL, mesenchymal MES, neural NEU, and proneural PN), based on the TCGA RNAseq and Agilent4502A datasets. GBM status: non-tumor n = 4, GBM n = 156; Grades: II n = 226, III n = 244, IV n = 150; IDH: WT n = 339, mut n = 27; Subtypes: CL n = 86, MES n = 96, NEU n = 111, PN n = 238.

(D) Kaplan-Meier curve of the probability of survival for n = 244 GBM patients with low vs high expression of MLKL, using optimal cut-off settings in the TCGA dataset.

(E) Protein lysates from tumor and control (healthy) human brain tissue biopsies were analyzed by immunoblot for MLKL protein expression (arrow). The hashtag symbol indicates a non-specific signal. GAPDH serves as a loading control.

(F) MLKL protein expression was assessed in three patient-derived Glioblastoma Stem-like Cells from mesenchymal (GSC1 and GSC4) and classical (GSC9) subtypes. GAPDH serves as a loading control. Immunoblots are representative of at least n = 3. t-test and ANOVA, *p < 0.05, **p < 0.01, ***p < 0.001, ns not-significant.

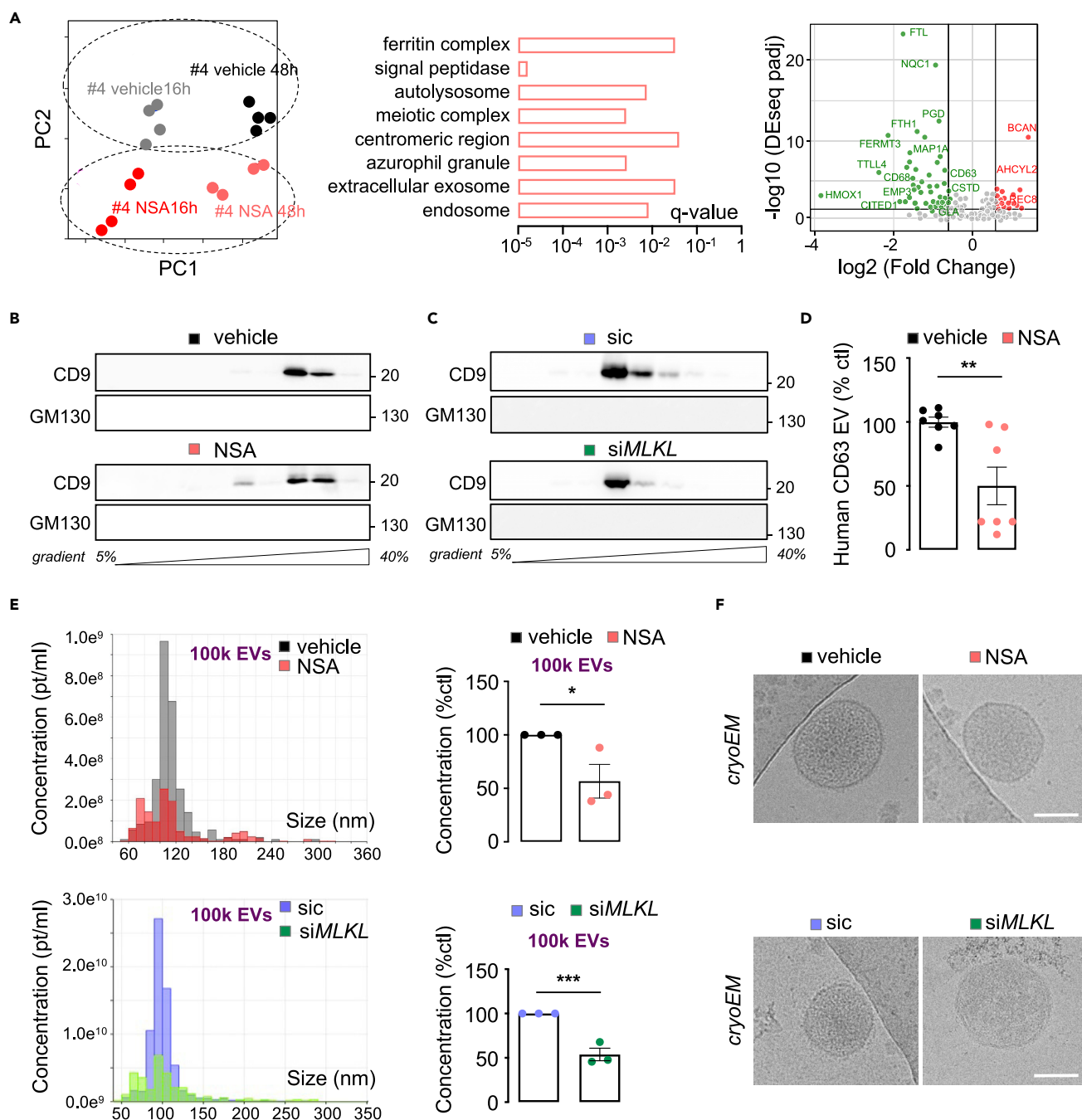


Figure 2. MLKL inhibition impairs the constitutive release of extracellular vesicles

(A) Transcriptomic analysis by 3' Sequencing RNA Profiling (3'SRP) of Glioblastoma Stem-like Cells (GSC4) treated with vehicle (DMSO) and NSA (5 μ M) for 16h and 48h. The left panel represents the principal component analysis (PCA) of quadruplicates. Middle panel, analysis of over- or under-represented (q-value) GO terms. Right panel, specific genes under- (green) or over- (red) expressed in NSA-treated GSC4.

(B and C) Density gradient analysis by immunoblot of 100k EVs for the EV marker CD9 and the putative cellular contaminant GM130, in the 10 collected fractions from top to bottom. EVs were isolated from GSC4 treated for 48h with vehicle (DMSO) and the MLKL inhibitor NSA (5 μ M) (b). Alternatively, EVs were isolated from GSC9 that received RNA duplexes targeting MLKL (siMLKL) and non-silencing duplexes (sic) (c). $n = 2$, respectively.

(D) Quantification by ELISA of 100k EVs isolated from a 48h-old vehicle and NSA-treated GSC4, $n = 7$.

Figure 2. Continued

(E) Representative diagrams of size distribution and particle concentration of small EVs (100k) isolated from GSC4 that received either vehicle (DMSO) and NSA (upper panel) or sic and siMLKL (bottom panel), as measured with tunable resistive pulse sensing analysis (TRPS, qNano, IZON). Histograms quantifying relative particle concentration (% of control) in EVs (100k) were shown (right panels). pt = particle, n = 3.

(F) Representative cryo-electron microscopy (cryoEM) images of 100k fractions from MLKL-inhibited and -silenced GSC9 as in (e). Scale bars: 100 nm. Mann-Whitney test, *p < 0.05, **p < 0.01, ***p < 0.001.

Glioblastoma stem-like cells are resistant to necroptosis

Because MLKL is a crucial effector of necroptosis (Sun et al., 2012; Zhao et al., 2012), we next assessed whether this form of cell death occurs in GSCs. Necroptosis can be ignited by TNF α (T) in cells, in which both apoptosis and NF- κ B-dependent pro-survival pathways are blocked, for instance with the pan-caspase inhibitor QVD (Q) and the SMAC-mimetic birinapant (S), respectively (Douanne et al., 2019). Accordingly, in Jurkat T lymphocytes, TQS treatment caused a loss in phosphatidylserine asymmetry, together with a rupture of the plasma membrane, evidenced by Annexin V binding and PI incorporation, further culminating in marked cell death (Figures S2A and S2B). As expected, pretreatment with the necroptosis inhibitor Necrostatin-1 (Nec) largely rescued Jurkat viability. In sharp contrast, three patient-derived GSCs described earlier (Harford-Wright et al., 2017), namely GSC1, GSC4, and GSC9, remained largely unaffected upon TQS challenge (Figures S2A and S2B). Yet, GSCs treated with TNF α displayed hallmarks of NF- κ B activation such as NF- κ B p65 and I κ B α phosphorylation, and degradation of total I κ B α (Figure S2C). To explore in-depth the mechanisms underlying the failure of necroptosis induction, the expression of receptor-interacting protein kinases RIPK1 and RIPK3 (Sun et al., 2012), the upstream activators of MLKL, was monitored as epigenetic regulations downregulate RIPK3 in several cancers (Koo et al., 2015; Moriwaki et al., 2015; Wang et al., 2020). Although RIPK1 expression was readily observed in GSCs, neither RIPK3 mRNA nor protein was detected in the three patient-derived GSCs tested (Figures S2D and S2E). Of note, in the absence of RIPK3, a subset of MLKL was found under a phosphorylated form, detected at steady-state, both with phosphate-affinity electrophoresis (Phos-tag) and immunofluorescence (Figures S2F and S2G). Accordingly, MLKL can be phosphorylated on several amino acids (T357, S358, S125, Y376 and other residues yet to be determined) by RIPK3 and other kinases to serve cell death and non-cell death functions, respectively (Dai et al., 2020; Gong et al., 2017; Yoon et al., 2017). In conclusion, our data reveals that the inability of patient-derived GSCs to complete the necroptotic program likely results from the lack of RIPK3 expression.

MLKL controls the biogenesis of extracellular vesicles in glioblastoma stem-like cells

In addition to its lethal pore-forming activity, MLKL participates in membrane trafficking and release of EVs, as well as necroptosis-associated vesicle formation (Douanne et al., 2019; Gong et al., 2017; Yoon et al., 2017; Zargarian et al., 2017). Because EVs orchestrate GBM pathogenesis and aggressiveness (André-Grégoire and Gavard, 2017), we next explored the role of the pseudokinase in EV biogenesis in viable, proliferating GSCs. First, transcriptomic analysis of cellular RNA was carried out in GSCs treated with necrosulfonamide (NSA) (Sun et al., 2012), a widely used MLKL inhibitor, at early and late time points (i.e. 16h and 48h) (Figure 2A). Principal component analysis showed that the first variance can be explained by the duration of NSA exposure (early time point on the left vs 48h on the right), whereas the second variance discriminated between untreated and treated samples (DMSO above versus NSA bottom; Figure 2A, left panel). Differentially expressed genes (q-value) were then hierarchically categorized based on their Gene Ontology, unmasking an organelle trafficking signature, with some of the most typical genes highlighted on the volcano plot (Figure 2A, middle and right panels) (Table S1). This supports the notion that NSA treatment might indeed alter intracellular trafficking.

To next assess its role in EV release, MLKL was either blocked pharmacologically with NSA or silenced by RNA interference. EVs were then isolated from GSC supernatants by differential ultracentrifugation (Théry et al., 2006), as depicted in Figure S3A and detailed under the EV-TRACK ID#EV210024 following international recommendations (Théry et al., 2018). Immunoblot analysis validated the separation procedure with the presence of two vesicular proteins, namely the transmembrane tetraspanin CD63 and the intravesicular accessory protein of the ESCRT machinery Alix, in the 100k fraction, together with the absence of the Golgi marker GM130 (Figure S3B). Meanwhile, typical features of EVs were detectable in electron microscopy imaging (Figure S3C). Separation by density gradient, followed by immunoblotting analysis for the tetraspanin CD9 revealed the distribution of EVs in the expected fractions (Figures 2B and 2C). The level of CD9-positive particles was found reduced when cells were either challenged with the MLKL inhibitor NSA (Figure 2B) or silenced for MLKL (Figure 2C). Indeed, MLKL inhibition was accompanied by a decrease

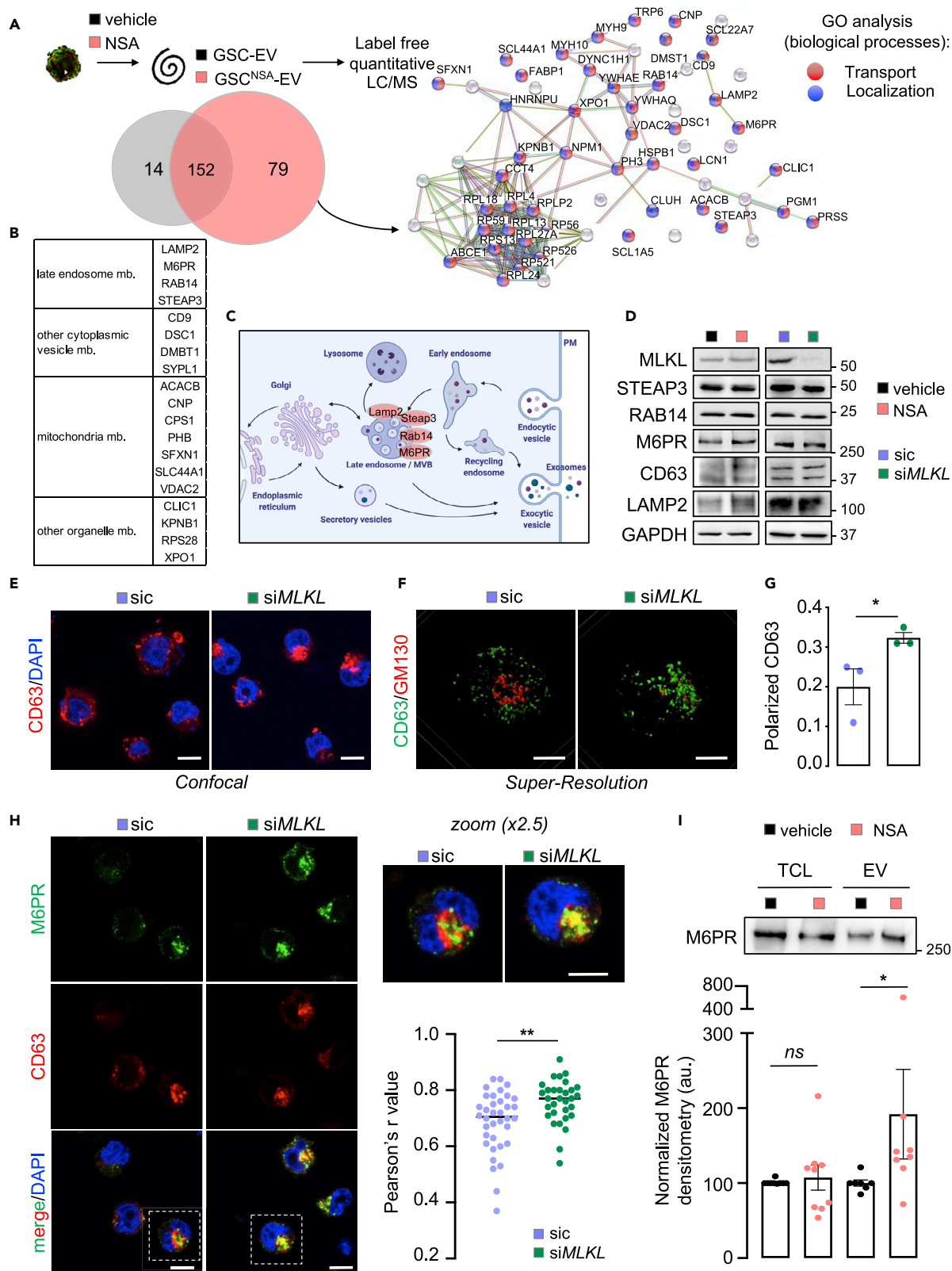


Figure 3. MLKL regulates the release of extracellular vesicles from glioblastoma stem-like cells

(A) Mass spectrometry analysis (LC-MS/MS) of the protein content of Extracellular Vesicles (EVs) isolated from Glioblastoma Stem-like Cells (GSC4) treated with vehicle (DMSO) and the MLKL inhibitor NSA (5 μ M) for 48h. The right panel shows STRING analysis of the 79 proteins detected only in EVs isolated from NSA-treated cells. Main gene ontology (GO) biological processes are highlighted in red (Transport) and blue (Localization).

(B) Table highlighting differential proteins (79 and 14) from (a) regarding Cellular Component focusing on organelles and vesicles membranes associated proteins.

(C) Intracellular trafficking routes focusing on EV biogenesis with differentially detected proteins associated to late endosome Cellular Component in EVs from (b).

(D) GSC4 were either challenged with DMSO and NSA for 48h or transfected with non-silencing (sic) and MLKL targeting RNA duplexes (siMLKL) for 72h prior analyses of the indicated proteins by immunoblot. GAPDH serves as a loading control.

(E) Representative confocal images of GSC4 transfected with sic and siMLKL for 72h, fixed, and immunostained for CD63. Nuclei were counterstained with DAPI (blue). Scale bars: 10 μ m, n = 3.

(F) Super-resolution structured illumination microscopy (SIM) was performed to analyze CD63 distribution in sic and siMLKL transfected GSC4. GM130 stained Golgi. Scale bars: 4 μ m, n = 2.

(G) Polarized immunostaining of CD63 was counted from panel (e) (n > 10 per sample, in three independent experiments).

(H) Representative confocal images of GSC9 transfected with sic and siMLKL for 72h, fixed, and immunostained for M6PR (green) and CD63 (red). Nuclei were counterstained with DAPI (blue). Scale bars: 10 μ m, n = 3. A 2.5x zoom is shown on the right panel together with Pearson's r correlation factor for n = 31 and n = 36 cells, respectively, from 3 independent experiments.

(I) GSC9 were challenged with vehicle (DMSO) and NSA and EVs were collected 48h later. Immunoblot for M6PR was performed in total cell lysates (TCL) and 100k fractions (EV). Normalized densitometric analysis is shown as the mean \pm s.e.m. for 8–9 independent experiments. All immunoblots are representative of at least n = 3. Mann-Whitney and t-tests, *p < 0.05, **p < 0.01, ns not-significant.

in the abundance of EVs, as measured by human CD63 ELISA (Figure 2D), typically marking endoplasmic-derived exosomes (van Niel et al., 2018). Single-particle tracking analysis was next deployed using tunable resistive pulse sensing (TRPS) technology (qNANO) to measure particle concentration of the EV preparations. TRPS measurements unmasked a reduced abundance of EVs when MLKL is pharmacologically hampered (Figure 2E). Likewise, MLKL silencing led to an overall reduction in the concentration of EVs from the 100k pellets (Figure 2E), thus mirroring the MLKL blockade phenotype. The morphology of isolated EVs was nonetheless rather similar in both conditions, as observed by cryo-EM, which preserved their native state as dehydration and chemical fixatives were omitted (Figure 2F). Of note, both the quality and quantity of EVs recovered in the 10k pellets were not altered (Figure S3D). Of interest, the concentration in EVs emanating from sister DGCs, in which MLKL expression is barely detectable (Figures S1B and S1C), remained largely unaffected by MLKL pharmacological inhibition with NSA (Figures S1D and S1E). As expected by the reported functions of RAB27 A/B in vesicular trafficking (Ostrowski et al., 2010; Figures S4A–S4C), a similar trend in EV concentration was observed in RAB27-silenced samples (Figures S4A–S4C). Overall, our data reinforce the idea of an alternate function of MLKL in the biogenesis of EVs in GSCs, independent of its role in necroptosis.

To gain further insights into how MLKL controls EV release, we next carried out a mass-spectrometry-based comparative analysis of the protein cargoes in EVs isolated from naive and NSA-challenged GSCs (Figure 3A and Table S2, 48h treatment). Known and predicted protein-protein interaction networks, as well as enriched pathways were then analyzed using the STRING open data source. This revealed that NSA treatment enriched the content of EVs towards proteins involved in biological processes associated with transport and localization, suggesting that MLKL inhibition might relate to EV processing and/or release (Figure 3A). Reinforcing this idea, large structures budding at the plasma membrane, as well as abnormal enlarged and unfilled multi-vesicular bodies (MVB) were imaged via electron microscopy in NSA-treated GSCs (Figure S5A).

Candidates highlighted in the proteomic analysis point toward an amendment in intracellular transport and localization, rather than tumor growth and expansion. However, the level of expression and the subcellular localization of intracellular organelle components, including endosomes, lysosomes, and Golgi were not overtly modified on MLKL inhibition and silencing (Figures S5B and S5C). Of note, the endoplasmic reticulum/Golgi secretory pathway was not affected by MLKL deletion in GSCs as measured by Gaussia luciferase glow assay (Figure S5D). Next, an in-depth analysis of the differential cargo (i.e. 14 proteins down and 79 proteins up in NSA-EVs as compared to vehicle-EVs) was performed with a focus on organelles and vesicle membrane-associated proteins (Figure 3B). This highlighted four proteins associated with MVB and late endosomes, namely LAMP2, M6PR, RAB14, and STEAP3 (Figures 3B and 3C). However, their abundance remained even in whole-cell lysates on either NSA treatment or MLKL silencing (Figure 3D). This set of data prompted us to analyze the intracellular localization of CD63, a classical tetraspanin marker for

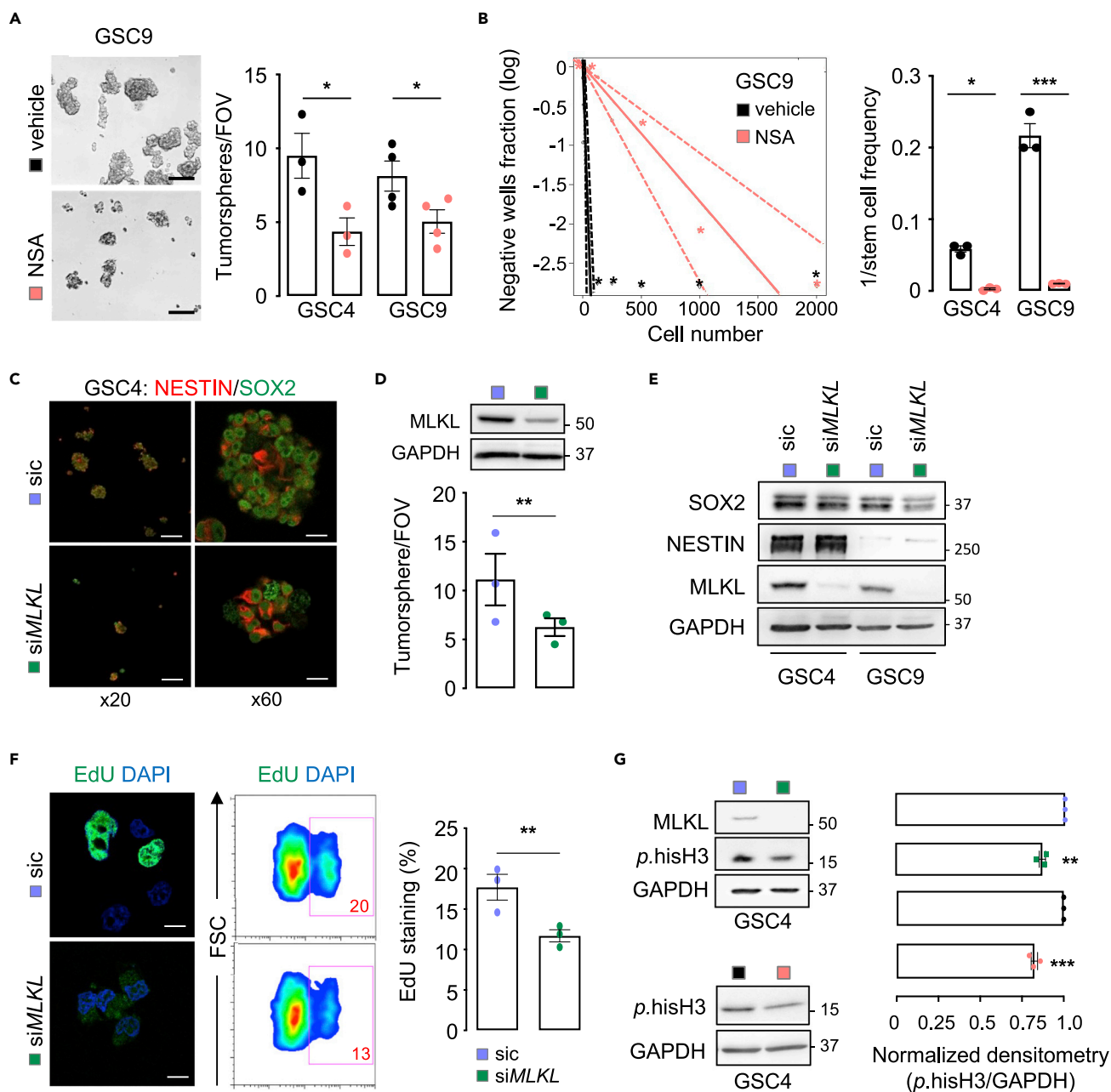


Figure 4. MLKL inhibition reduces glioblastoma stem-like cell expansion in vitro

(A) Representative bright-field images of Glioblastoma Stem-like Cells (GSC9) treated with vehicle (DMSO) or the MLKL inhibitor NSA (5 μ M) for 48h. Scale bars: 100 μ m. Tumorsphere formation assay (manually counted per field of view, FOV) was performed in GSC4 and GSC9 in response to vehicle and NSA treatments for 4 days.

(B) Extreme limiting dilution assay (ELDA) in response to vehicle and NSA for 14 days. Left panel, representative linear regression plot for DMSO and NSA-treated GSC9. Right panel, ELDA estimation of the stem cell frequency in GSC4 and GSC9.

(C) Representative confocal images of GSC4 transfected with non-silencing (sic) and MLKL targeting RNA duplexes (siMLKL) and analyzed for NESTIN (red) and SOX2 (green) stemness markers after 72h. Scale bars $\times 20$: 100 μ m; $\times 60$: 16 μ m.

(D) Upper panel, the knockdown efficiency of MLKL was verified in transfected GSC4 after 72h by immunoblotting of MLKL. GAPDH serves as a loading control. Lower panel, tumorsphere formation assay (manually counted per field of view, FOV) for 4 days in sic and siMLKL transfected GSC4.

(E) The expression of SOX2 and NESTIN was evaluated by immunoblot in GSC4 and GSC9 transfected with sic and siMLKL for 72h. GAPDH serves as a loading control.

Figure 4. Continued

(F) Left panel, representative confocal images of EdU incorporation (green) in sic and siMLKL GSC4. Nuclei were counterstained with DAPI (blue). Scale bars: 10 μ m. Middle panel, representative flow cytometry analysis of EdU incorporation. Right panel, the percentage of EdU-positive cells was quantified from the middle panel in three independent experiments.

(G) Protein lysates from sic and siMLKL GSC4 (72h), as well as NSA-treated GSC4 (48h) were analyzed by immunoblot for phospho-Histone H3 (p.hisH3) and further quantified by densitometry (right panel), $n = 3$. MLKL knockdown was verified. GAPDH serves as a loading control. Data are representative of at least three independent experiments, unless otherwise stated. Mann-Whitney test, * $p < 0.05$, ** $p < 0.01$, *** $p < 0.001$.

EVs enriched in late endosomes and lysosomes (Ostrowski et al., 2010), and of M6PR, a transmembrane glycoprotein that shuttles between Golgi and endosomal compartments and tags proteins toward lysosomes (Brown et al., 1986; Figures 3E–3H). Our confocal and super-resolution microscopy analysis unveiled relocation and clustering of CD63 in GSCs, knocked down for MLKL (Figures 3E–3G). Moreover, we found that M6PR accumulated in CD63-positive intracellular compartments in MLKL-silenced cells (Figure 3H). Together with M6PR enrichment in EVs on MLKL inhibition (Figures 3A and 3I and Table S2), this suggests that M6PR is rerouted toward EVs, therefore supporting the idea that intracellular trafficking is defective when MLKL is impaired.

Interfering with MLKL reduces GSC expansion

To evaluate the functional impact of interfering with MLKL in GSCs, we next deployed a triad of complementary interfering approaches: pharmacological inhibitor, siRNA, and targeted protein degradation. NSA administration hindered spheroid aspect, size, and formation in two patient-derived GSCs (Figure 4A). The ability to self-renew was further halted as estimated by extreme limiting dilution assay and stem cell frequency index (Figure 4B). Real-time, automated imaging confirmed the impairment in tumorsphere formation on NSA treatment (up to 4 days, VideoS1). We also observed a reduction in the size and number of tumor spheroids from MLKL-silenced cells, although the level of expression of the classical markers for stemness NESTIN and SOX2 were not overtly changed (Figures 4C–4E). Because defective tumorsphere formation might be linked to proliferation, EdU incorporation and histone H3 phosphorylation were assessed in MLKL siRNA-transfected GSCs. Both confocal images and flow cytometry demonstrated that proliferation was reduced in MLKL knocked down cells (Figure 4F). This was also true for Histone H3 phosphorylation (Figure 4G), indicating a defect in cell cycle progression through mitosis. Mirroring siRNA experiments, proliferation was also reduced on MLKL inhibition with NSA (Figure 4G). We next adapted an antibody-targeting degradation approach, named trim-away (Clift et al., 2017), to directly and acutely deplete MLKL protein (Figure 5C, left panel). Supporting our results with RNA interference, the targeted elimination of MLKL protein caused an increase in cell death (Figure 5C, right panel). This death was accompanied by a marked activation of caspase-3 and caspase-8 and by the cleavage of caspase substrates, including PARP and Gasdermin E (Figure 5D). Blocking MLKL leads to a reduction in viability and an increase in cell death, as evidenced by reduced metabolic activity and increased phosphatidylserine exposure, respectively (Figures 5A and 5B). This was however not the case in differentiated sister cells, that express a lower amount of MLKL (Figures 5A and S1). In addition, MLKL knockdown mimicked the silencing of RAB27A/B secretory proteins in terms of viability and cell death (Figures S4D and S4E).

We then evaluated whether the viability defect could be rescued by adding back EVs from control, untreated sibling GSCs. Of note, 10k and 100k EV fractions were equally internalized in control and MLKL-silenced GSCs, therefore suggesting no overt loss of EV uptake in GSCs (Figure S6A). However, the co-culture with EVs could not restore the cell viability of MLKL-inhibited and -silenced cells (Figures S6B and S6C). Conversely, EVs isolated from NSA-treated and MLKL-silenced cells failed to induce cell death (Figures S6B and S6C), overall suggesting an intrinsic defect rather than autocrine/paracrine action of EVs in GSCs.

Lastly, we combined MLKL targeting with the alkylating agent TMZ, which is the standard-of-care chemotherapeutic drug to which GSCs are largely resistant *in vitro* and *in vivo* (André-Grégoire et al., 2018). As expected, treatment with TMZ induced the phosphorylation of ATM (Caporali et al., 2004), and this was not altered by blocking MLKL (Figure 5E). Of interest, cell death was increased when MLKL inhibition was combined with TMZ administration (Figure 5E), suggesting a possible additive and/or permissive action of MLKL blockade on TMZ challenge. Thus, blocking MLKL opposed GSC expansion *in vitro*.

Pharmacological targeting of MLKL *in vivo* inhibits glioblastoma tumor growth

Our results prompted us to evaluate the effect of MLKL inhibition in an orthotopic *in vivo* model of GBM in nude mice (Figures S7A–S7F) (Harford-Wright et al., 2017; Lenting et al., 2017). Noticeably, NSA blocks human but not murine MLKL, therefore inferring that the drug effects are most likely related to the targeting of

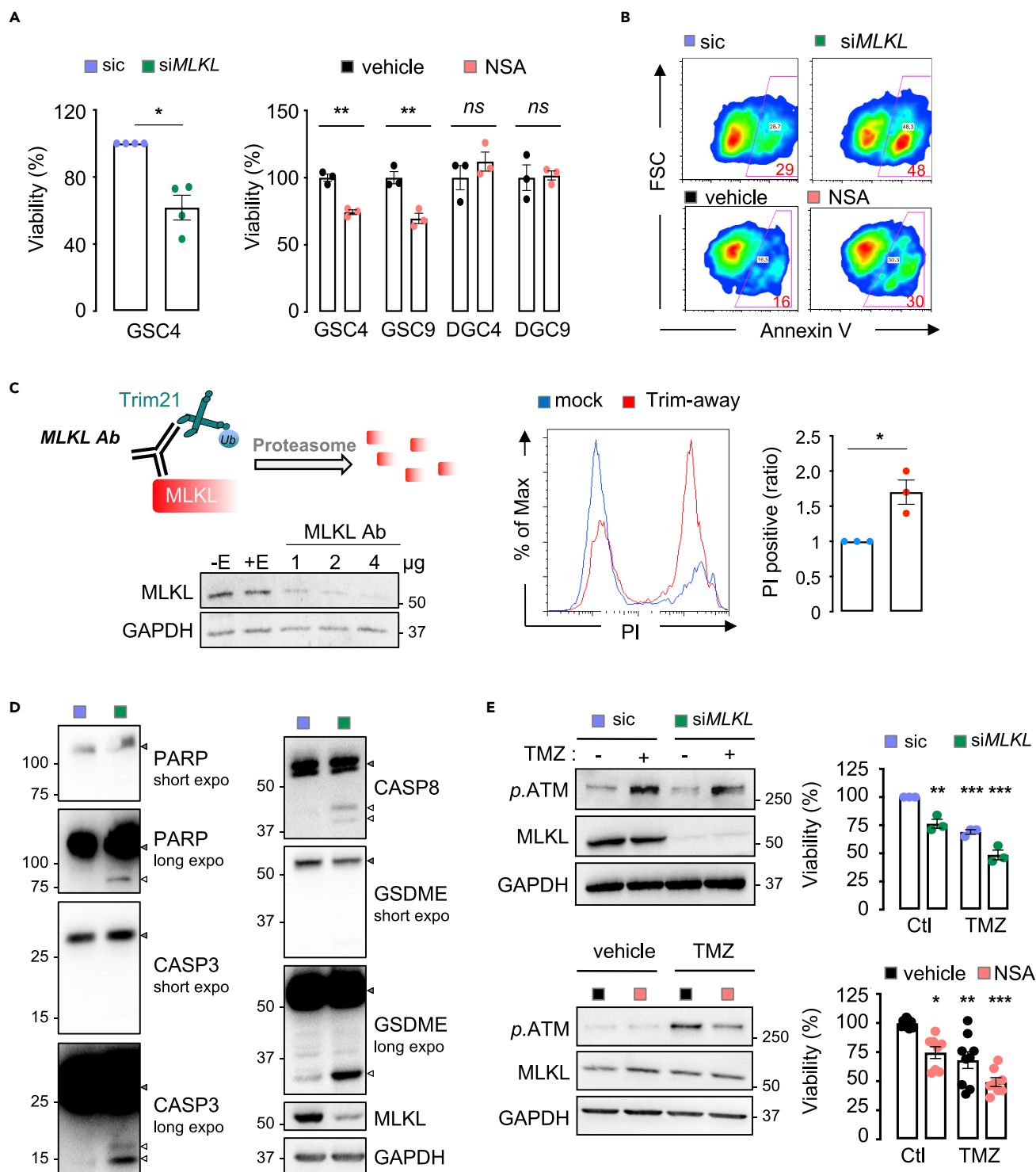


Figure 5. MLKL inhibition increases glioblastoma stem-like cell death and potentiates temozolomide action in vitro

(A) UptiBlue viability assays were performed in non-silencing (sic)- and MLKL targeting RNA duplexes (siMLKL)-transfected Glioblastoma Stem-like Cells (GSC4, left panel) and CellTiter-Glo viability assay of GSC4 and GSC9 and their corresponding Differentiated Glioblastoma Cells (DGC4 and DGC9) after 48h treatment with vehicle (DMSO) and the MLKL inhibitor NSA (5 μ M, right panel), $n = 3$.

(B) Representative flow cytometry analysis of the cell death marker Annexin V surface staining on either sic and siMLKL or vehicle and NSA-treated GSC4, as in (a).

Figure 5. Continued

(C) Left panel, endogenous MLKL protein was directly targeted for proteasome degradation by Trim-away technique using electroporation of MLKL antibody (Ab). MLKL levels were analyzed in GSC4 by immunoblot 16h after electroporation of increasing quantities of MLKL antibody (Ab). GAPDH serves as a loading control. "E" means electroporation. Right panel, quantification by flow cytometry of propidium iodide (PI) incorporation in GSC4 after MLKL trim-away (16h, 4 μ g). Histograms show the ratio between PI-positive and total cells. $n = 3$.

(D) Cell death pathways were analyzed in sic and siMLKL GSC9 monitoring the processing of the indicated proteins (plain arrows indicate full-length proteins, empty arrows indicate cleaved proteins). MLKL knockdown was verified. $n = 3$.

(E) Left panels, immunoblot analysis of the phosphorylation of ATM (alkylation signature, p.ATM) in GSC4 treated with the standard-of-care alkylating agent temozolomide (TMZ, 100 μ M, 48h) on MLKL silencing (upper panel) and inhibition (bottom panel). MLKL and GAPDH serve as internal and loading controls. Right panels, UptiBlue viability assays after 48h in GSC4, as in left panels. $n = 3$ and $n = 8$ respectively. Data are representative of at least three independent experiments, unless otherwise stated. Mann-Whitney test and one-way ANOVA, * $p < 0.05$, ** $p < 0.01$, *** $p < 0.001$, ns not-significant.

xenografted human patient-derived GBM cells and not the host cells in these experimental settings. First, tumor-free mice were administered 5 mg/kg of NSA tri-weekly for 4 weeks by intraperitoneal route (Figure 6A). The gross animal examination did not reveal alterations in the general health status between healthy animals that received either NSA or vehicle (Figure 6B). The same was true with complete blood count (Table S3). Although the weights of the heart and kidneys did not seem to suffer from NSA challenge, livers appeared slimmer, although plasmatic levels of ASAT and ALAT were unchanged, overall suggesting no overt adverse effects of NSA administration in mice (Figures 6C and 6D).

To gain further insights into the therapeutic potential of MLKL inhibition in GBM, nude mice were implanted with GFP-Luc-expressing GSC9 into the striatum and treated with NSA (5 mg/kg) three times a week, starting one-week post-grafting in randomized animals (Figure 6E). Tumor progression was monitored with bioluminescence imaging once a week together with signs of morbidity (Figure 6E). Tumor-emanating bioluminescence was quantitatively reduced on NSA intraperitoneal administration at end-point and over-time, suggesting a reduced in tumor growth (Figures 6F–6I). This was indeed associated with shrinking tumor mass in NSA-challenged animals, as evidenced by hematoxylin/eosin staining (Figure 6G), whereas NESTIN-positive tumor cells and ISOLECTIN-labeled vessels were readily visible in both cases (Figure 6H). Importantly, NSA injection significantly improved the overall survival of tumor-bearing mice compared to their vehicle-treated counterparts (Figure 6J), suggesting an overall reduction in tumor burden. To control whether this beneficial action was accompanied by a change in EV release from the tumor grafts, murine blood was collected at sacrifice, mouse host and human donor circulating EVs were isolated and the abundance of EVs from human tumor cell origin was estimated with human CD63 ELISA (Figure 6K). In keeping with the idea that vesiclemia, i.e., the concentration of EVs in plasma (Sabbagh et al., 2020), correlated with tumor evolution (Osti et al., 2019; Sabbagh et al., 2021), the abundance of human origin EVs was dampened in animals that received human-targeting pharmacological compound NSA (Figure 6K). Mirroring the *in vitro* situation, the level of M6PR was superior in the EV fractions from NSA-challenged mice peripheral blood, as compared to plasmatic EVs from vehicle-receiving animals (Figure 6K). Collectively, these *in vivo* data provide a strong basis for an instrumental role of MLKL in the production of tumor-derived EVs and GBM progression.

DISCUSSION

EVs operate as instrumental conveyors in cancer settlement and progression (Sabbagh et al., 2020). They orchestrate the delivery of tumor-emanating signaling cues in the local environment and at distance, and therefore contribute to diseases. Likewise, GBM cells constitutively release a large amount of EVs, playing important roles in gliomagenesis, resistance to treatments, and cell-to-cell communication within the tumor soil (Al-Nedawi et al., 2008; André-Grégoire and Gavard, 2017; Garnier et al., 2018; Harshyne et al., 2016; Luhtala et al., 2017; Skog et al., 2008; Treps et al., 2016, 2017; deVrij et al., 2015; Yin et al., 2019; Zeng et al., 2018; Zhang et al., 2019). In this context, interfering with EV-based communication might impede tumor growth. However, the direct impact of blocking EV biogenesis in the source cell is not fully elucidated. Here, we provide the proof-of-concept that targeting MLKL and affecting MLKL-dependent release of GBM EVs are associated with a reduction in GBM cell growth *in vitro* and *in vivo*.

During necroptotic cell death, MLKL phosphorylation by RIPK3 drives its oligomerization and insertion in the plasma membrane, thereby forming lytic pores (Cai et al., 2014; Douanne et al., 2019; Murphy et al., 2013; Sun et al., 2012). Although several compounds were shown to trigger necroptosis in GBM cell lines *in vitro* (Ding et al., 2019; Huang et al., 2013; Melo-Lima et al., 2014; Miki et al., 2015; Yu et al., 2020; Zhou et al., 2020), our data show that this is not the case with patient-derived GSCs, as they lack RIPK3

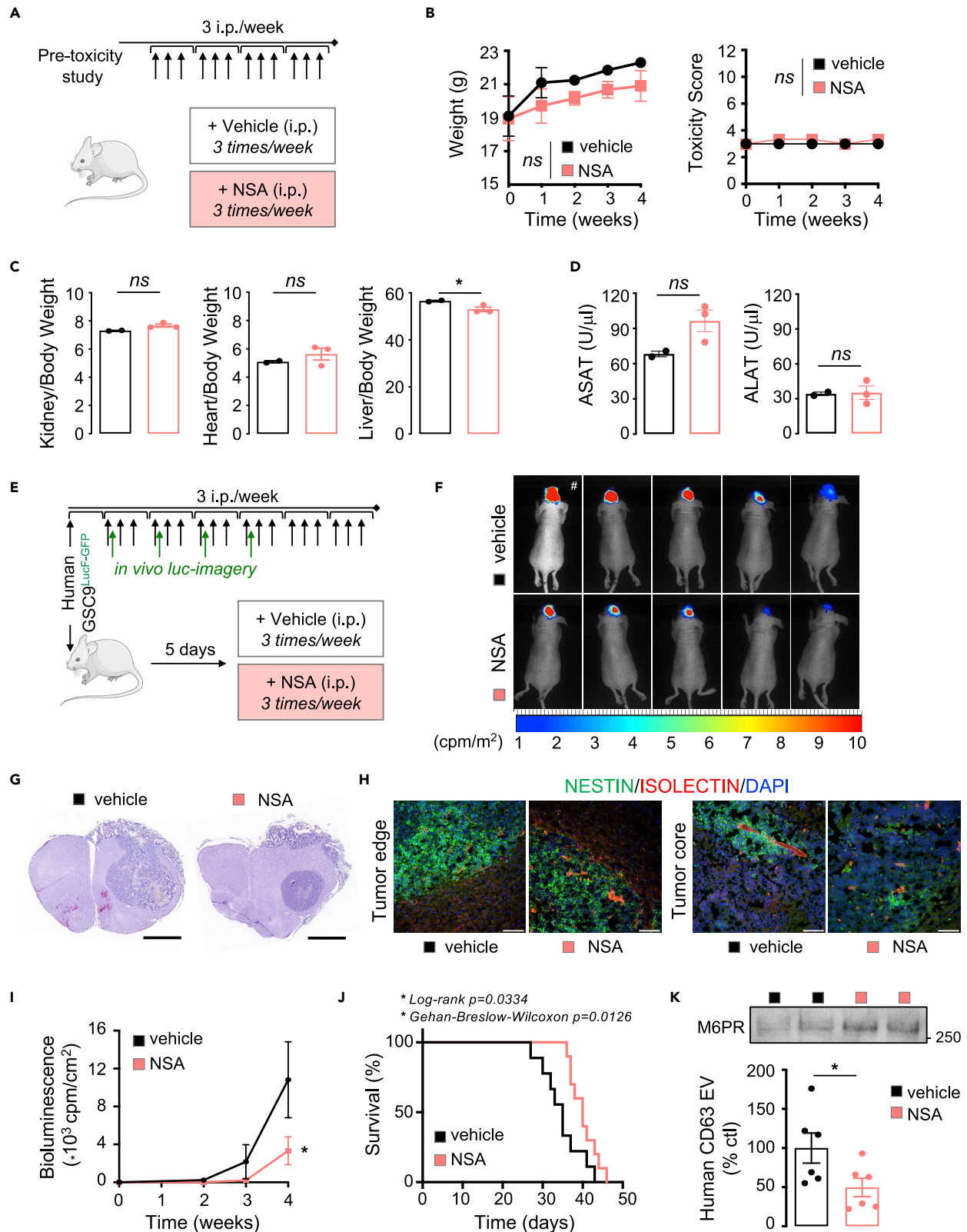


Figure 6. NSA administration slows down tumor growth *in vivo*

- (A) Diagram of the protocol for evaluation of NSA tolerance *in vivo* in mice.
- (B) Follow-up of the body weight (left panel) and behavior and general health parameters (toxicity score, right panel) in tumor-free mice treated with vehicle (DMSO) and NSA for 4 weeks (intraperitoneal, i.p. 5 mg/kg, 3 times/week), n = 2 (vehicle) and = 3 (NSA).
- (C) Kidney, heart, and liver were observed and weighted at sacrifice (week 4) for toxicity assessment, n = 2 (vehicle) and = 3 (NSA).
- (D) Liver function assessment using the transaminase ASAT and ALAT measurements in plasma from vehicle and NSA-treated mice for 4 weeks, n = 2 (vehicle) and = 3 (NSA).
- (E) Diagram of implantation of patient-derived Glioblastoma Stem-like Cells (luciferase-GFP-expressing GSC9), and treatment regime with vehicle and NSA (intraperitoneal, i.p. 5 mg/kg, 3 times/week). Follow-up of tumor growth is performed via luciferase (Luc)-based live imaging.
- (F) Representative bioluminescence images of brain tumors at week 4 (except #, done at week 3 before death), n = 5.
- (G) Representative hematoxylin/eosin staining is shown for end-point tumors in vehicle and NSA-treated mice. Scale bars: 2 mm.
- (H) Representative images from ISOLECTIN-labeled blood vessels (red) and NESTIN-stained tumor cells (green) on frozen sections from end-point tumors as in (g), showing both the tumor edge and core. Nuclei were counterstained with DAPI (blue). Scale bars: 100 μ m.
- (I) Quantification of luminescence (count per minute, cpm/cm²) in mice treated with vehicle and NSA, as depicted in panel (f), n = 5.
- (J) Kaplan-Meier survival curve of mice treated with vehicle and NSA, n = 10 from two independent experiments with five mice.
- (K) Peripheral blood from vehicle- (DMSO, black) and NSA- (pink) animals was collected at end-points and analyzed by western blot to evaluate the M6PR protein abundance (upper panel, n = 3 mice) and by human CD63-ELISA (bottom panel, n = 6 mice) to assess the vesiclemia. Data are expressed as the percentage of vehicle, from two independent experiments. Mann-Whitney test and two-way ANOVA, *p < 0.05 and ns not-significant.

expression. This later finding fits with the idea that RIPK3 expression is lost in most cancer cells and tissues because of epigenetic changes (Koo et al., 2015; Moriwaki et al., 2015; Wang et al., 2020). Indeed, the downregulation of RIPK3 owing to genomic methylation of its promoter blocks, at least partially, necroptosis-induced cell death by several chemotherapeutic agents (Koo et al., 2015; Moriwaki et al., 2015; Wang et al., 2020). The low expression of RIPK3 is associated with a poor prognosis in esophageal squamous cell carcinoma (Sun et al., 2018), whereas RIPK3 status was recently proposed as a prognostic marker for low-grade glioma (Vergara et al., 2020). Thus, epigenetic regulation of RIPK3 gene expression in GSCs might be hijacked to shield against MLKL-dependent necroptotic cell death.

In viable cells, MLKL was shown to undergo phosphorylation, independently of RIPK3, and to associate with intracellular vesicles, where it regulates constitutive endosomal trafficking and extrusion of EVs (Yoon et al., 2017). Whether MLKL undergoes phosphorylation and oligomerization to regulate EV genesis in GSCs is still under investigation. Weak but sustainable phosphorylation of MLKL was detected in GSCs. Also, our results with NSA, which prevents MLKL multimerization via covalent interaction with human MLKL residue Cys86 while sparing its phosphorylation, suggest that similar mechanisms might be at play in GSCs.

Multomics analysis of the EV content, as well as a detailed look at the global structure of organelles, suggest that the loss of MLKL function corroborates with the defective multivesicular body (MVB) maturation route. This step is described to require the RAB27A/B small GTPases, which facilitate the trafficking of MVBs toward the cell periphery, as well as their docking and fusion to the plasma membrane (Douanne et al., 2019; Ostrowski et al., 2010; van Niel et al., 2018). MLKL interference phenocopies RAB27A/B silencing in patient-derived GSCs, in terms of EV release and cell viability (Bobrie et al., 2012; van Solinge et al., 2020). Likewise, altering RAB27A/B functions was shown to reduce migration and invasiveness in a model of a glioma cell line, by manipulating lysosomal cathepsin D exocytosis (Liu et al., 2012). Here, proteomic analysis suggests that LAMP2 accumulated in NSA-derived EVs. However, although lysosomes do not seem to be overtly affected by MLKL inhibition in GSCs, further studies will decipher whether MLKL blockade shapes lysosome function and/or autophagy, as identified vulnerability points in GBM (Jacobs et al., 2020; Shingu et al., 2017). In the same vein, additional protein candidates might emerge from our proteomic study, such as the ones enriched in NSA-derived EVs and associated with MVB membranes. For example, MLKL deficiency leads to M6PR mislocalization in cells, along with its accumulation in EVs, which might be linked to the multivesicular endosomal trafficking defects (late endosome/pre-lysosome stage), as previously reported (Hirst et al., 1998). Also, RAB14 colocalizes with CD63 (Kuijl et al., 2013) and plays an important role in exosome biogenesis (Maziveyi et al., 2019). This regulation of exosome secretion by RAB14 was shown to participate in the control of breast cancer tumor growth (Maziveyi et al., 2019). Thus, the MVB maturation route of EVs emerges as the mainstream on which MLKL inhibition might operate to affect tumor growth.

In keeping with the idea of limiting EV-dependent communication within the tumor microenvironment, MLKL might emerge as a potential druggable target. First, *mlkl* knockout mice are viable without obvious abnormalities, suggesting, therefore, that silencing MLKL *in vivo* does not exert any major deleterious effects in healthy

mice (Wu et al., 2013). The maximal nontoxic dose of NSA injected intraperitoneally in mice was determined at 20 mg/kg (Rathkey et al., 2018). In addition, the small size of sulfonamide compounds suggests that NSA may cross the blood-brain barrier in mice even when administered via systemic routes (Bartzatt et al., 2010). Here, we used a chimeric model in which human patient-derived cells are transplanted into immunosuppressed mouse brains. Because NSA targets human, but not murine, MLKL protein (Sun et al., 2012), it is tempting to speculate that NSA impairs directly human tumor cell growth within the brain, reinforcing the idea that NSA crosses the blood-brain barrier in the xenograft models. Of note, the NSA challenge not only reduced the concentration of circulating EVs of human origin in the peripheral blood of intracranial tumor-bearing mice but also tumor burden, culminating in the extension of their survival. Targeting EVs *in vivo* to reduce tumor growth has already been proposed. For example in GBM, miR-1 overexpression in GSCs was able to modify EV protein cargoes and ultimately reduce tumorigenicity, invasiveness, and angiogenesis *in vivo* in xenografted mice (Bronisz et al., 2014). In addition, RAB27A silencing resulted in decreased primary tumor growth and lung dissemination of metastatic carcinoma (Bobrie et al., 2012; van Solinge et al., 2020). Furthermore, monitoring the level of circulating EVs in the bloodstream might reflect tumor size. Indeed, GBM patients have increased vesiclemia (André-Grégoire et al., 2018; Sabbagh et al., 2021), while resection normalized these values (Osti et al., 2019). Thus, the level of plasmatic EVs may assist in the clinical management of GBM patients, and/or anticipate recurrence as a companion diagnostic tool. Overall, our work unveils the potential of interfering with EV biogenesis as a new combined therapy to sensitize GBM cells to death.

Limitations of the study

Our current study indicates that both inhibition and depletion of MLKL led to a reduction in the release of EVs and resulted in the loss of fitness of GBM patient-derived stem-like cells *in vitro*. Yet, adding back control sibling EVs did not rescue this phenotype, and EVs from MLKL-inhibited moribund cells were not toxic. This suggests that blocking EV release intrinsically damaged GSC expansion. However, we have not fully elucidated how MLKL operates in this context. Moreover, the pharmacological inhibition of human MLKL slowed down *in vivo* tumor growth in immunocompromised xenografted animals. Given the high degree of MLKL expression in myeloid cells, future studies will be required to unravel how blocking MLKL in both the tumor cells and microenvironment impacts GBM progression.

STAR★METHODS

Detailed methods are provided in the online version of this paper and include the following:

- KEY RESOURCES TABLE
- RESOURCE AVAILABILITY
 - Lead contact
 - Materials availability
 - Data and code availability
- EXPERIMENTAL MODEL AND SUBJECT DETAILS
 - Animals
 - Cell culture
- METHOD DETAILS
 - Glioblastoma xenografts and safety evaluation of NSA
 - The Cancer Genome Atlas (TCGA) analysis
 - MLKL targeting
 - Immunoblotting
 - Antibodies
 - Isolation of extracellular vesicles (EVs)
 - Quantification of particles
 - Cryo-electron microscopy
 - Confocal and super-resolution microscopy
 - Proteomic analysis of EVs
 - Transcriptomic analysis
 - Stemness assays
 - Proliferation and cytotoxicity assays
 - Flow cytometry
 - Chemicals
 - RT-PCR and-qPCR

- siRNA
- Phos-tag
- Uptake and co-culture with EVs
- IncuCyte
- Electron microscopy
- **QUANTIFICATION AND STATISTICAL ANALYSIS**

SUPPLEMENTAL INFORMATION

Supplemental information can be found online at <https://doi.org/10.1016/j.isci.2022.105118>.

ACKNOWLEDGMENTS

We are grateful to past and present SOAP team members, especially Sarah Delalleau (Université de Nantes, INSERM, CNRS, France). We also thank François Guillonnet, Cédric Broussard, and Virginie Salnot from Plateforme Proteom'IC 3P5, Université de Paris, Institut Cochin, Paris, France for performing sample preparation and data acquisition and analysis, Joëlle Veziers (SC3M, CHU Nantes, France) for image acquisition, Valérie Trichet (Université de Nantes, France) for eGFP-Luc plasmids, and the Genomics and Bioinformatics Core Facility of Nantes (GenoBiRD, Biogenouest, IFB) for their technical assistance with 3'SRP analysis. We would like to acknowledge the core-facilities from SFR Santé François Bonamy, Nantes, France (MicroPICell ANR-10-INBS-04, Cytocell, Therassay, and UTE IRS-UN) and Cathy Royer (plateforme d'imagerie in vitro, CNRS UPS3156, Strasbourg, France).

This work was supported by Fondation de France (GAG), Fondation pour la Recherche Médicale (Equipe labellisée DEQ20180339184), Fondation ARC contre le Cancer (PJA to JG and NB), Institut National du Cancer (INCa PLBIO 2019-151, INCa PLBIO 2019-291, INCa PAIR-CEREB INCa_16285), Ligue nationale contre le cancer (Equipe labellisée) et comités de Loire-Atlantique, Maine et Loire, Vendée, Ile-et-Vilaine (JG, NB). TD received a fellowship from Nantes Métropole, AT and SR from Fondation ARC, KAJ from Nantes Métropole and Fondation ARC, CM from Ligue Régionale contre le Cancer and Région Pays-de-la-Loire. The team is part of the SIRIC ILIAD (INCA-DGOS-Inserm_12558).

AUTHOR CONTRIBUTIONS

G.A.G., N.B., and J.G. – Conception and design, acquisition of data, analysis, and interpretation of data, drafting the article. C.M., T.D., S.R., F.S., A.T., K.T., K.A.J., C.B., A.D., A.M.L., F.M.G.C., I.B., V.H., and J.G.G. – Acquisition of data, analysis, and interpretation of data. All authors approved the manuscript.

DECLARATION OF INTERESTS

The authors declare no competing interests.

INCLUSION AND DIVERSITY

We support inclusive, diverse, and equitable conduct of research.

Received: March 11, 2022

Revised: August 4, 2022

Accepted: September 8, 2022

Published: October 21, 2022

REFERENCES

- Al-Nedawi, K., Meehan, B., Micallef, J., Lhotak, V., May, L., Guha, A., and Rak, J. (2008). Intercellular transfer of the oncogenic receptor EGFRvIII by microvesicles derived from tumour cells. *Nat. Cell Biol.* 10, 619–624. <https://doi.org/10.1038/ncb1725>.
- André-Grégoire, G., and Gavard, J. (2017). Spitting out the demons: extracellular vesicles in glioblastoma. *Cell Adhes. Migr.* 11, 164–172. <https://doi.org/10.1080/19336918.2016.1247145>.
- André-Grégoire, G., Bidère, N., and Gavard, J. (2018). Temozolomide affects extracellular vesicles released by glioblastoma cells. *Biochimie* 155, 11–15. <https://doi.org/10.1016/j.biochi.2018.02.007>.
- Bao, S., Wu, Q., McLendon, R.E., Hao, Y., Shi, Q., Hjelmeland, A.B., Dewhirst, M.W., Bigner, D.D., and Rich, J.N. (2006). Glioma stem cells promote radioresistance by preferential activation of the DNA damage response. *Nature* 444, 756–760. <https://doi.org/10.1038/nature05236>.
- Bartzatt, R., Cirillo, S.L.G., and Cirillo, J.D. (2010). Sulfonamide agents for treatment of Staphylococcus MRSA and MSSA infections of the central nervous system. *Cent. Nerv. Syst. Agents Med. Chem.* 10, 84–90. <https://doi.org/10.2174/187152410790780109>.
- Bobrie, A., Krumeich, S., Rey, F., Recchi, C., Moita, L.F., Seabra, M.C., Ostrowski, M., and Théry, C. (2012). Rab27a supports exosome-dependent and -independent mechanisms that modify the tumor microenvironment and can

promote tumor progression. *Cancer Res.* 72, 4920–4930. <https://doi.org/10.1158/0008-5472.CAN-12-0925>.

Bowman, R.L., Wang, Q., Carro, A., Verhaak, R.G.W., and Squatrito, M. (2017). Gliovis data portal for visualization and analysis of brain tumor expression datasets. *Neuro Oncol.* 19, 139–141. <https://doi.org/10.1093/neuonc/now247>.

Bronisz, A., Wang, Y., Nowicki, M.O., Peruzzi, P., Ansari, K., Ogawa, D., Balaj, L., De Rienzo, G., Mineo, M., Nakano, I., et al. (2014). Extracellular vesicles modulate the glioblastoma microenvironment via a tumor suppression signaling network directed by miR-1. *Cancer Res.* 74, 738–750. <https://doi.org/10.1158/0008-5472.CAN-13-2650>.

Brown, W.J., Goodhouse, J., and Farquhar, M.G. (1986). Mannose-6-phosphate receptors for lysosomal enzymes cycle between the Golgi complex and endosomes. *J. Cell Biol.* 103, 1235–1247. <https://doi.org/10.1083/jcb.103.4.1235>.

Cai, Z., Jitkaew, S., Zhao, J., Chiang, H.-C., Choksi, S., Liu, J., Ward, Y., Wu, L.-G., and Liu, Z.-G. (2014). Plasma membrane translocation of trimerized MLKL protein is required for TNF-induced necroptosis. *Nat. Cell Biol.* 16, 55–65. <https://doi.org/10.1038/ncb2883>.

Caporali, S., Zhong, H., Scheuer, T., Catterall, W.A., Bonmassar, E., Jiricny, J., and D'Atri, S. (2004). DNA damage induced by temozolomide signals to both ATM and ATR: role of the mismatch repair system. *Mol. Pharmacol.* 66, 761–769. <https://doi.org/10.1124/mol.66.3>.

Chen, J., Li, Y., Yu, T.-S., McKay, R.M., Burns, D.K., Kernie, S.G., and Parada, L.F. (2012). A restricted cell population propagates glioblastoma growth after chemotherapy. *Nature* 488, 522–526. <https://doi.org/10.1038/nature11287>.

Clift, D., McEwan, W.A., Labzin, L.I., Konieczny, V., Mogessie, B., James, L.C., and Schuh, M. (2017). A method for the acute and rapid degradation of endogenous proteins. *Cell* 171, 1692–1706.e18. <https://doi.org/10.1016/j.cell.2017.10.033>.

Clift, D., So, C., McEwan, W.A., James, L.C., and Schuh, M. (2018). Acute and rapid degradation of endogenous proteins by Trim-Away. *Nat. Protoc.* 13, 2149–2175.

Dai, J., Zhang, C., Guo, L., He, H., Jiang, K., Huang, Y., Zhang, X., Zhang, H., Wei, W., Zhang, Y., et al. (2020). A necroptotic-independent function of MLKL in regulating endothelial cell adhesion molecule expression. *Cell Death Dis.* 11, 282. <https://doi.org/10.1038/s41419-020-2483-3>.

de Vrij, J., Maas, S.L.N., Kwappenberg, K.M.C., Schnoor, R., Kleijn, A., Dekker, L., Luider, T.M., de Witte, L.D., Litjens, M., van Strien, M.E., et al. (2015). Glioblastoma-derived extracellular vesicles modify the phenotype of monocytic cells. *Int. J. Cancer* 137, 1630–1642. <https://doi.org/10.1002/ijc.29521>.

Ding, Y., He, C., Lu, S., Wang, X., Wang, C., Wang, L., Zhang, J., Piao, M., Chi, G., Luo, Y., et al. (2019). MLKL contributes to shikonin-induced glioma cell necroptosis via promotion of chromatinolysis. *Cancer Lett.* 467, 58–71. <https://doi.org/10.1016/j.canlet.2019.09.007>.

Douanne, T., André-Grégoire, G., Trillet, K., Thys, A., Papin, A., Feyeux, M., Hulin, P., Chiron, D., Gavard, J., and Bidère, N. (2019). Pannexin-1 limits the production of proinflammatory cytokines during necroptosis. *EMBO Rep.* 20, e47840. <https://doi.org/10.15252/embr.201947840>.

EV-TRACK Consortium, Mestdagh, P., Akay, Ö., Anckaert, J., Baetens, T., Bertier, L., Boere, J., Bremer, M., Byrd, J.B., Cheng, L., Daveloose, D., et al. (2017). EV-TRACK: transparent reporting and centralizing knowledge in extracellular vesicle research. *Nat. Methods* 14, 228–232. <https://doi.org/10.1038/nmeth.4185>.

Gao, X., Zhang, Z., Mashimo, T., Shen, B., Nyagilo, J., Wang, H., Wang, Y., Liu, Z., Mulgaonkar, A., Hu, X.-L., et al. (2020). Gliomas interact with non-glioma brain cells via extracellular vesicles. *Cell Rep.* 30, 2489–2500.e5. <https://doi.org/10.1016/j.celrep.2020.01.089>.

Garnier, D., Meehan, B., Kislinger, T., Daniel, P., Sinha, A., Abdulkarim, B., Nakano, I., and Rak, J. (2018). Divergent evolution of temozolomide resistance in glioblastoma stem cells is reflected in extracellular vesicles and coupled with radiosensitization. *Neuro Oncol.* 20, 236–248. <https://doi.org/10.1093/neuonc/nox142>.

Gimple, R.C., Bhargava, S., Dixit, D., and Rich, J.N. (2019). Glioblastoma stem cells: lessons from the tumor hierarchy in a lethal cancer. *Genes Dev.* 33, 591–609. <https://doi.org/10.1101/gad.324301.119>.

Gong, Y.-N., Guy, C., Olason, H., Becker, J.U., Yang, M., Fitzgerald, P., Linkermann, A., and Green, D.R. (2017). ESCRT-III acts downstream of MLKL to regulate necroptotic cell death and its consequences. *Cell* 169, 286–300.e16. <https://doi.org/10.1016/j.cell.2017.03.020>.

Harford-Wright, E., Andre-Gregoire, G., Jacobs, K.A., Treps, L., Le Gonidec, S., Leclair, H.M., Gonzalez-Diest, S., Roux, Q., Guillonnet, F., Loussouarn, D., et al. (2017). Pharmacological targeting of apelin impairs glioblastoma growth. *Brain* 140, 2939–2954. <https://doi.org/10.1093/brain/awx253>.

Harshyne, L.A., Nasca, B.J., Kenyon, L.C., Andrews, D.W., and Hooper, D.C. (2016). Serum exosomes and cytokines promote a T-helper cell type 2 environment in the peripheral blood of glioblastoma patients. *Neuro Oncol.* 18, 206–215. <https://doi.org/10.1093/neuonc/nov107>.

Hirst, J., Futter, C.E., and Hopkins, C.R. (1998). The kinetics of mannose 6-phosphate receptor trafficking in the endocytic pathway in Hep-2 cells: the receptor enters and rapidly leaves multivesicular endosomes without accumulating in a prelysosomal compartment. *Mol. Biol. Cell* 9, 809–816. <https://doi.org/10.1091/mbc.9.4.809>.

Hu, Y., and Smyth, G.K. (2009). ELDA: extreme limiting dilution analysis for comparing depleted and enriched populations in stem cell and other assays. *J. Immunol. Methods* 347, 70–78. <https://doi.org/10.1016/j.jim.2009.06.008>.

Huang, C., Luo, Y., Zhao, J., Yang, F., Zhao, H., Fan, W., and Ge, P. (2013). Shikonin kills glioma cells through necroptosis mediated by RIP-1. *PLoS One* 8, e66326. <https://doi.org/10.1371/journal.pone.0066326>.

Jacobs, K.A., André-Grégoire, G., Maghe, C., Thys, A., Li, Y., Harford-Wright, E., Trillet, K., Douanne, T., Alves Nicolau, C., Frénel, J.S., et al. (2020). Paracaspase MALT1 regulates glioma cell survival by controlling endo-lysosome homeostasis. *EMBO J.* 39, e102030. <https://doi.org/10.15252/emboj.2019102030>.

Karlsson, M., Zhang, C., Méar, L., Zhong, W., Digre, A., Katona, B., Sjöstedt, E., Butler, L., Odeberg, J., Dusart, P., et al. (2021). A single-cell type transcriptomics map of human tissues. *Sci. Adv.* 7, eabh2169. <https://doi.org/10.1126/sciadv.abh2169>.

Koo, G.-B., Morgan, M.J., Lee, D.-G., Kim, W.-J., Yoon, J.-H., Koo, J.S., Kim, S.I., Kim, S.J., Son, M.K., Hong, S.S., et al. (2015). Methylation-dependent loss of RIP3 expression in cancer represses programmed necrosis in response to chemotherapeutics. *Cell Res.* 25, 707–725. <https://doi.org/10.1038/cr.2015.56>.

Kuijl, C., Pilli, M., Alahari, S.K., Janssen, H., Khoo, P.-S., Ervin, K.E., Calero, M., Jonnalagadda, S., Scheller, R.H., Neefjes, J., and Junutula, J.R. (2013). Rac and Rab GTPases dual effector Nischarin regulates vesicle maturation to facilitate survival of intracellular bacteria. *EMBO J.* 32, 713–727. <https://doi.org/10.1038/emboj.2013.10>.

Lenting, K., Verhaak, R., ter Laan, M., Wesseling, P., and Leenders, W. (2017). Glioma: experimental models and reality. *Acta Neuropathol.* 133, 263–282. <https://doi.org/10.1007/s00401-017-1671-4>.

Liu, Y., Zhou, Y., and Zhu, K. (2012). Inhibition of glioma cell lysosome exocytosis inhibits glioma invasion. *PLoS One* 7, e45910. <https://doi.org/10.1371/journal.pone.0045910>.

Luhtala, N., Aslanian, A., Yates, J.R., and Hunter, T. (2017). Secreted glioblastoma nanovesicles contain intracellular signaling proteins and active Ras incorporated in a farnesylation-dependent manner. *J. Biol. Chem.* 292, 611–628. <https://doi.org/10.1074/jbc.M116.747618>.

Maziveyi, M., Dong, S., Baranwal, S., Mehrnezhad, A., Rathinam, R., Huckaba, T.M., Mercante, D.E., Park, K., and Alahari, S.K. (2019). Exosomes from nischarin-expressing cells reduce breast cancer cell motility and tumor growth. *Cancer Res.* 79, 2152–2166. <https://doi.org/10.1158/0008-5472.CAN-18-0842>.

Melo-Lima, S., Celeste Lopes, M., and Mollinedo, F. (2014). Necroptosis is associated with low procaspase-8 and active RIPK1 and -3 in human glioma cells. *Oncoscience* 1, 649–664. <https://doi.org/10.18632/oncoscience.89>.

Miki, Y., Akimoto, J., Moritake, K., Hironaka, C., and Fujiwara, Y. (2015). Photodynamic therapy using talaporfin sodium induces concentration-dependent programmed necrosis in human glioblastoma T98G cells. *Lasers Med. Sci.* 30, 1739–1745. <https://doi.org/10.1007/s10103-015-1783-9>.

Moriwaki, K., Bertin, J., Gough, P.J., Orlowski, G.M., and Chan, F.K.M. (2015). Differential roles of RIPK1 and RIPK3 in TNF-induced necroptosis and chemotherapeutic agent-induced cell death. *Cell Death Dis.* 6, e1636. <https://doi.org/10.1038/cddis.2015.16>.

- Murphy, J.M., Czabotar, P.E., Hildebrand, J.M., Lucet, I.S., Zhang, J.-G., Alvarez-Diaz, S., Lewis, R., Lalaoui, N., Metcalf, D., Webb, A.I., et al. (2013). The pseudokinase MLKL mediates necroptosis via a molecular switch mechanism. *Immunity* 39, 443–453. <https://doi.org/10.1016/j.immuni.2013.06.018>.
- Osti, D., Del Bene, M., Rappa, G., Santos, M., Matafora, V., Richichi, C., Faletti, S., Beznoussenko, G.V., Mironov, A., Bachi, A., et al. (2019). Clinical significance of extracellular vesicles in plasma from glioblastoma patients. *Clin. Cancer Res.* 25, 266–276. <https://doi.org/10.1158/1078-0432.CCR-18-1941>.
- Ostrowski, M., Carmo, N.B., Krumeich, S., Fanget, I., Raposo, G., Savina, A., Moita, C.F., Schauer, K., Hume, A.N., Freitas, R.P., et al. (2010). Rab27a and Rab27b control different steps of the exosome secretion pathway. *Nat. Cell Biol.* 12, 19–30. [sup pp 1-13. https://doi.org/10.1038/ncb2000](https://doi.org/10.1038/ncb2000).
- Pastrana, D.V., Tolstov, Y.L., Becker, J.C., Moore, P.S., Chang, Y., and Buck, C.B. (2009). Quantitation of human seroresponsiveness to Merkel cell polyomavirus. *PLoS Pathog.* 5, e1000578. <https://doi.org/10.1371/journal.ppat.1000578>.
- Quezada, C., Torres, Á., Niechi, I., Uribe, D., Contreras-Duarte, S., Toledo, F., San Martín, R., Gutiérrez, J., and Sobrevía, L. (2018). Role of extracellular vesicles in glioma progression. *Mol. Aspects Med.* 60, 38–51. <https://doi.org/10.1016/j.mam.2017.12.003>.
- Rathkey, J.K., Zhao, J., Liu, Z., Chen, Y., Yang, J., Kondolf, H.C., Benson, B.L., Chirieleison, S.M., Huang, A.Y., Dubyak, G.R., et al. (2018). Chemical disruption of the pyroptotic pore-forming protein gasdermin D inhibits inflammatory cell death and sepsis. *Sci. Immunol.* 3, eaat2738. <https://doi.org/10.1126/sciimmunol.aat2738>.
- Sabbagh, Q., André-Grégoire, G., Alves-Nicolau, C., Dupont, A., Bidère, N., Jouglar, E., Guével, L., Frénel, J.S., and Gavard, J. (2021). The von Willebrand factor stamps plasmatic extracellular vesicles from glioblastoma patients. *Sci. Rep.* 11, 22792. <https://doi.org/10.1038/s41598-021-02254-7>.
- Sabbagh, Q., Andre-Gregoire, G., Guevel, L., and Gavard, J. (2020). Vesiclemia: counting on extracellular vesicles for glioblastoma patients. *Oncogene* 39, 6043–6052. <https://doi.org/10.1038/s41388-020-01420-x>.
- Shingu, T., Ho, A.L., Yuan, L., Zhou, X., Dai, C., Zheng, S., Wang, Q., Zhong, Y., Chang, Q., Horner, J.W., et al. (2017). Qki deficiency maintains stemness of glioma stem cells in suboptimal environment by downregulating endolysosomal degradation. *Nat. Genet.* 49, 75–86. <https://doi.org/10.1038/ng.3711>.
- Shlomovitz, I., Erlich, Z., Arad, G., Edry-Botzer, L., Zargarian, S., Cohen, H., Manko, T., Ofir-Birin, Y., Cooks, T., Regev-Rudski, N., and Gerlic, M. (2021). Proteomic analysis of necroptotic extracellular vesicles. *Cell Death Dis.* 12, 1059. <https://doi.org/10.1038/s41419-021-04317-z>.
- Singh, S.K., Hawkins, C., Clarke, I.D., Squire, J.A., Bayani, J., Hide, T., Henkelman, R.M., Cusimano, M.D., and Dirks, P.B. (2004). Identification of human brain tumour initiating cells. *Nature* 429, 396–401. <https://doi.org/10.1038/nature03128>.
- Skog, J., Würdinger, T., van Rijn, S., Meijer, D.H., Gainche, L., Sena-Esteves, M., Curry, W.T., Carter, B.S., Krichevsky, A.M., and Breakefield, X.O. (2008). Glioblastoma microvesicles transport RNA and proteins that promote tumour growth and provide diagnostic biomarkers. *Nat. Cell Biol.* 10, 1470–1476. <https://doi.org/10.1038/ncb1800>.
- Stupp, R., Mason, W.P., van den Bent, M.J., Weller, M., Fisher, B., Taphoorn, M.J.B., Belanger, K., Brandes, A.A., Marosi, C., Bogdahn, U., et al. (2005). Radiotherapy plus concomitant and adjuvant temozolomide for glioblastoma. *N. Engl. J. Med.* 352, 987–996. <https://doi.org/10.1056/NEJMoa043330>.
- Sun, L., Wang, H., Wang, Z., He, S., Chen, S., Liao, D., Wang, L., Yan, J., Liu, W., Lei, X., and Wang, X. (2012). Mixed lineage kinase domain-like protein mediates necrosis signaling downstream of RIP3 kinase. *Cell* 148, 213–227. <https://doi.org/10.1016/j.cell.2011.11.031>.
- Sun, Y., Zhai, L., Ma, S., Zhang, C., Zhao, L., Li, N., Xu, Y., Zhang, T., Guo, Z., Zhang, H., et al. (2018). Down-regulation of RIP3 potentiates cisplatin chemoresistance by triggering HSP90-ERK pathway mediated DNA repair in esophageal squamous cell carcinoma. *Cancer Lett.* 418, 97–108. <https://doi.org/10.1016/j.canlet.2018.01.022>.
- Théry, C., Amigorena, S., Raposo, G., and Clayton, A. (2006). Isolation and characterization of exosomes from cell culture supernatants and biological fluids. *Curr. Protoc. Cell Biol.* 30, 3.22.1–3.22.29. <https://doi.org/10.1002/0471143030.cb0322s30>.
- Théry, C., Witwer, K.W., Aikawa, E., Alcaraz, M.J., Anderson, J.D., Andriantsohaina, R., Antoniou, A., Arab, T., Archer, F., Atkin-Smith, G.K., et al. (2018). Minimal information for studies of extracellular vesicles 2018 (MISEV2018): a position statement of the International Society for Extracellular Vesicles and update of the MISEV2014 guidelines. *J. Extracell. Vesicles* 7, 1535750. <https://doi.org/10.1080/20013078.2018.1535750>.
- Treps, L., Edmond, S., Harford-Wright, E., Galan-Moya, E.M., Schmitt, A., Azzi, S., Citerne, A., Bidère, N., Ricard, D., and Gavard, J. (2016). Extracellular vesicle-transported Semaphorin3A promotes vascular permeability in glioblastoma. *Oncogene* 35, 2615–2623. <https://doi.org/10.1038/ncr.2015.317>.
- Treps, L., Perret, R., Edmond, S., Ricard, D., and Gavard, J. (2017). Glioblastoma stem-like cells secrete the pro-angiogenic VEGF-A factor in extracellular vesicles. *J. Extracell. Vesicles* 6, 1359479. <https://doi.org/10.1080/20013078.2017.1359479>.
- Van Deun, J., Mestdag, P., Sormunen, R., Cocquyt, V., Vermaelen, K., Vandesompele, J., Bracke, M., De Wever, O., and Hendrix, A. (2014). The impact of disparate isolation methods for extracellular vesicles on downstream RNA profiling. *J. Extracell. Vesicles* 3, 24858. <https://doi.org/10.3402/jev.v3.24858>.
- van Niel, G., D'Angelo, G., and Raposo, G. (2018). Shedding light on the cell biology of extracellular vesicles. *Nat. Rev. Mol. Cell Biol.* 19, 213–228. <https://doi.org/10.1038/nrm.2017.125>.
- van Solinge, T.S., Abels, E.R., van de Haar, L.L., Hanlon, K.S., Maas, S.L.N., Schnoor, R., de Vrij, J., Breakefield, X.O., and Broekman, M.L.D. (2020). Versatile role of Rab27a in glioma: effects on release of extracellular vesicles, cell viability, and tumor progression. *Front. Mol. Biosci.* 7, 554649. <https://doi.org/10.3389/fmolb.2020.554649>.
- Vergara, G.A., Eugenio, G.C., Malheiros, S.M.F., Victor, E.d.S., and Weinlich, R. (2020). RIPK3 is a novel prognostic marker for lower grade glioma and further enriches IDH mutational status subgrouping. *J. Neuro Oncol.* 147, 587–594. <https://doi.org/10.1007/s11060-020-03473-0>.
- Verhaak, R.G.W., Hoadley, K.A., Purdom, E., Wang, V., Qi, Y., Wilkerson, M.D., Miller, C.R., Ding, L., Golub, T., Mesirov, J.P., et al. (2010). Integrated genomic analysis identifies clinically relevant subtypes of glioblastoma characterized by abnormalities in PDGFRA, IDH1, EGFR, and NF1. *Cancer Cell* 17, 98–110. <https://doi.org/10.1016/j.ccr.2009.12.020>.
- Wang, Q., Wang, P., Zhang, L., Tessema, M., Bai, L., Xu, X., Li, Q., Zheng, X., Saxton, B., Chen, W., et al. (2020). Epigenetic regulation of RIP3 suppresses necroptosis and increases resistance to chemotherapy in Non-Small cell lung cancer. *Transl. Oncol.* 13, 372–382. <https://doi.org/10.1016/j.tranon.2019.11.011>.
- Wu, J., Huang, Z., Ren, J., Zhang, Z., He, P., Li, Y., Ma, J., Chen, W., Zhang, Y., Zhou, X., et al. (2013). Mkl knockout mice demonstrate the indispensable role of Mkl in necroptosis. *Cell Res.* 23, 994–1006. <https://doi.org/10.1038/cr.2013.91>.
- Yan, H., Parsons, D.W., Jin, G., McLendon, R., Rasheed, B.A., Yuan, W., Kos, I., Batnig-Haberle, I., Jones, S., Riggins, G.J., et al. (2009). IDH1 and IDH2 mutations in gliomas. *N. Engl. J. Med.* 360, 765–773. <https://doi.org/10.1056/NEJMoa0808710>.
- Yin, J., Zeng, A., Zhang, Z., Shi, Z., Yan, W., and You, Y. (2019). Exosomal transfer of miR-1238 contributes to temozolomide-resistance in glioblastoma. *EBioMedicine* 42, 238–251. <https://doi.org/10.1016/j.ebiom.2019.03.016>.
- Ying, Z., Pan, C., Shao, T., Liu, L., Li, L., Guo, D., Zhang, S., Yuan, T., Cao, R., Jiang, Z., et al. (2018). Mixed lineage kinase domain-like protein MLKL breaks down myelin following nerve injury. *Mol. Cell* 72, 457–468.e5. <https://doi.org/10.1016/j.molcel.2018.09.011>.
- Yoon, S., Kovalenko, A., Bogdanov, K., and Wallach, D. (2017). MLKL, the protein that mediates necroptosis, also regulates endosomal trafficking and extracellular vesicle generation. *Immunity* 47, 51–65.e7. <https://doi.org/10.1016/j.immuni.2017.06.001>.
- Yu, J., Zhong, B., Jin, L., Hou, Y., Ai, N., Ge, W., Li, L., Liu, S., Lu, J.-J., and Chen, X. (2020). 2-Methoxy-6-acetyl-7-methyljuglone (MAM) induced programmed necrosis in glioblastoma by targeting NAD(P)H: quinone oxidoreductase 1 (NQO1). *Free Radic. Biol. Med.* 152, 336–347. <https://doi.org/10.1016/j.freeradbiomed.2020.03.026>.

Zargarian, S., Shlomovitz, I., Erlich, Z., Hourizadeh, A., Ofir-Birin, Y., Croker, B.A., Regev-Rudzki, N., Edry-Botzer, L., and Gerlic, M. (2017). Phosphatidylserine externalization, "necroptotic bodies" release, and phagocytosis during necroptosis. *PLoS Biol.* 15, e2002711. <https://doi.org/10.1371/journal.pbio.2002711>.

Zeng, A., Wei, Z., Yan, W., Yin, J., Huang, X., Zhou, X., Li, R., Shen, F., Wu, W., Wang, X., and You, Y. (2018). Exosomal transfer of miR-151a enhances chemosensitivity to temozolomide in

drug-resistant glioblastoma. *Cancer Lett.* 436, 10–21. <https://doi.org/10.1016/j.canlet.2018.08.004>.

Zhang, Z., Yin, J., Lu, C., Wei, Y., Zeng, A., and You, Y. (2019). Exosomal transfer of long non-coding RNA SBF2-AS1 enhances chemoresistance to temozolomide in glioblastoma. *J. Exp. Clin. Cancer Res.* 38, 166. <https://doi.org/10.1186/s13046-019-1139-6>.

Zhao, J., Jitkaew, S., Cai, Z., Choksi, S., Li, Q., Luo, J., and Liu, Z.-G. (2012). Mixed lineage

kinase domain-like is a key receptor interacting protein 3 downstream component of TNF-induced necrosis. *Proc. Natl. Acad. Sci. USA* 109, 5322–5327. <https://doi.org/10.1073/pnas.1200012109>.

Zhou, J., Li, G., Han, G., Feng, S., Liu, Y., Chen, J., Liu, C., Zhao, L., and Jin, F. (2020). Emodin induced necroptosis in the glioma cell line U251 via the TNF- α /RIP1/RIP3 pathway. *Invest. New Drugs* 38, 50–59. <https://doi.org/10.1007/s10637-019-00764-w>.

STAR★METHODS

KEY RESOURCES TABLE

REAGENT or RESOURCE	SOURCE	IDENTIFIER
Antibodies		
ALIX	BioLegend	Cat#634502; RRID: AB_2162471
Caspase-3	Cell Signaling Technology	Cat#9662; RRID: AB_331439
Caspase-8	Cell Signaling Technology	Cat#9746; RRID: AB_2275120
CD63	System Biosciences	Cat#EXOAB-CD63A-1; RRID: AB_2561274
CD63	BD Biosciences	Cat#556019; RRID: AB_396297
CD9	System Biosciences	Cat#EXOAB-CD9A-1; RRID: AB_2687469
cleaved-caspase 3	Cell Signaling Technology	Cat#9664; RRID: AB_2070042
EEA1	BD Biosciences	Cat#610456; RRID: AB_397829
eGFP	Merck Millipore	Cat#AB10145; RRID: AB_1587096
GAPDH	Santa Cruz Biotechnology	Cat#sc-32233; RRID: AB_627679
GM130	Abcam	Cat#ab52649; RRID: AB_880266
GSDME	Abcam	Cat#ab215191; RRID: AB_2737000
IκBα	Cell Signaling Technology	Cat#4814; RRID: AB_390781
LAMP2	Santa Cruz Biotechnology	Cat#sc-18822; RRID: AB_626858
M6PR	Cell Signaling Technology	Cat#14364; RRID: AB_2798462
M6PR	Abcam	Cat#ab2733; RRID: AB_2122792
MLKL	Cell Signaling Technology	Cat#14993; RRID: AB_2721822
MLKL	Abcam	Cat#ab211045
NESTIN	Merck Millipore	Cat#MAB5326; RRID: AB_2251134
P65	Santa Cruz Biotechnology	Cat#sc-372; RRID: AB_632037
PARP	Santa Cruz Biotechnology	Cat#sc-8007; RRID: AB_628105
phospho-ATM	Cell Signaling Technology	Cat#5883; RRID: AB_10835213
phospho-Histone H3	Cell Signaling Technology	Cat#3377; RRID: AB_1549592
phospho-IκBα	Cell Signaling Technology	Cat#9246; RRID: AB_2267145
phospho-MLKL	Abcam	Cat#187091; RRID: AB_2619685
phospho-p65	Cell Signaling Technology	Cat#3033; RRID: AB_331284
RAB14	Santa Cruz Biotechnology	Cat#sc-271401; RRID: AB_10610486
RAB27A	Cell Signaling Technology	Cat#95394; RRID: AB_2800247
RIPK1	BD Biosciences	Cat#551042; RRID: AB_394015
RIPK3	Cell Signaling Technology	Cat#13526; RRID: AB_2687467
SOX2	Merck Millipore	Cat#AB5603; RRID: AB_2286686
STEAP3	Abcam	Cat#ab151566
TUBULIN	Santa Cruz Biotechnology	Cat#sc-8035; RRID: AB_628408
Biological samples		
Patient-derived glioblastoma cells GSC1, GSC4, GSC9	Harford-Wright et al. (2017)	N/A
Human Brain (Normal) tissue lysate	GeneTex	Cat#GTX28771
Human Brain Whole Tissue Lysate (Adult Whole Tumor)	Novus Biologicals	Cat# NB820-59423

(Continued on next page)

Continued

REAGENT or RESOURCE	SOURCE	IDENTIFIER
Chemicals, peptides, and recombinant proteins		
Necro sulfamide	Abcam	Cat#ab143839; CAS: 432531-71-0
Temozolomide	Sigma-Aldrich	Cat#PHR1437; CAS: 85622-93-1
Q-VD-OPh	R&D Systems	Cat#OPH001
Birinapant	Selleck Chemicals	Cat#S7015; CAS: 1260251-31-7
TNF α	R&D Systems	Cat#210-TA
Necrostatin	Selleck Chemicals	Cat#S8037; CAS: 4311-88-0
Isolectin GS-IB4	Life Technologies	Cat#I21413
D-luciferin	Interchim	Cat#FP-M1224D; CAS: 115144-35-9
PKH-67	Sigma-Aldrich	Cat#MIDI67-1KT
Critical commercial assays		
ELISA kit for CD63	System Biosciences	Cat#ExoELISA-ULTRA CD63
Click-it EDU assay kit for flow cytometry	Life Technologies	Cat#C10424
Click-it EDU assay kit for cellular imaging	Life Technologies	Cat#C10337
UptiBlue Viable cell counting reagent	Interchim	Cat#UP669413
Gaussia Luciferase Glow assay kit	Life Technologies	Cat#16160
CellTiterGlo Cell Viability Assay	Promega	Cat#G9243
Annexin V/PI	Life Technologies	Cat#V13245
Deposited data		
3'SRP GSC9 vehicle versus NSA	This paper	N/A
Label-free proteomics from EVs isolated in the supernatants of vehicle and NSA-treated cells	This paper	N/A
Experimental models: Cell lines		
Jurkat T-cells E6.1	ATCC	Cat#TIB-152
Experimental models: Organisms/strains		
Mouse: Balb/c Nude (BALB/cAnNRj-Foxn1 nu/nu)	Janvier Labs	Cat#SM-BALNU-F
Oligonucleotides		
siRNA targeting human <i>MLKL</i> GCAACGCA UGCCUGUUUCACCCAUA	Life Technologies	Cat#HSS136796
Non-silencing low-GC RNA duplexes	Life Technologies	Cat#12935111
Mixture of siRNAs targeting human <i>RAB27A</i>	Sigma-Aldrich	Cat#EHU91501
siRNA targeting human <i>RAB27B</i> AAACGTGT GGTTTATAATGCA	This paper	N/A
Primers for human <i>MLKL</i> F: GCCACTGGAGATATCCCGTT R: CTTCTCCCAGCTTCTTGTC	This paper	N/A
Primers for human <i>SOX2</i> F: CAAAAATGGCCATGCAGTT R: AGTTGGGATCGAACAAAAGCTATT	This paper	N/A
Primers for human <i>TUBB3</i> F: CAGATGTTTCGATGCCAAGAA R: GGGATCCACTCCACGAAGTA	This paper	N/A
Primers for human <i>RIPK1</i> F: AGTGACTTCCTGGAGAGTG R: TCATCATCTTCGCCTCCTCC	This paper	N/A

(Continued on next page)

Continued

REAGENT or RESOURCE	SOURCE	IDENTIFIER
Primers for human <i>RIPK3</i> F: CTCTCTGCGAAAGGACCAAG R: TCGTAGCCCCACTTCCTATG	This paper	N/A
Primers for human <i>RAB27B</i> F: CTTGCGAGGCTGACCGA R: CCACACACTGTTCCATTGCG	This paper	N/A
Primers for human <i>ACTB</i> F: GGACTTCGAGCAAGAGATGG R: AGCACTGTGTTGGCGTACAG	This paper	N/A
Primers for human <i>HPRT1</i> F: TGACACTGGCAAACAATGCA R: GGTCTTTTACCAGCAAGCT	This paper	N/A
Recombinant DNA		
Mixture of pLNT-LucF/pFG12-eGFP	This paper	N/A
phGluc	Pastrana et al. (2009); Addgene	Cat#22522

RESOURCE AVAILABILITY**Lead contact**

Further information and requests for resources and reagents should be directed to and will be fulfilled by the lead contact, Julie Gavard at Julie.gavard@inserm.fr.

Materials availability

This study did not generate new unique reagents.

Data and code availability

All data reported in this paper will be shared by the [lead contact](#) upon request.

This study does not report original code.

All data generated or analyzed during this study are included in this article and its [supplemental information](#) files.

EXPERIMENTAL MODEL AND SUBJECT DETAILS**Animals**

Animal procedures were conducted in agreement with the European Convention for the Protection of Vertebrate Animals used for Experimental and other Scientific Purposes (ETS 123) and approved by the French Government (APAFIS#2016–2015092917067009). At all times, animals were allowed access to food and water *ad libitum* and were housed in a specific pathogen-free (SPF) environment with temperature and hygrometry controls on a 12h day-night cycle. Six-to-eight months old female Balb/c Nude (BALB/cAnNRj-Foxn1 nu/nu) mice (Janvier Labs) were used for xenografts and safety evaluation of necrosulfonamide (NSA) compound.

Cell culture

Patient-derived glioblastoma cells with stem-like properties (GSCs) were obtained from primary glioblastoma resection, by dissociating tumor biopsies using the MACS Dissociator (Miltenyi). They were characterized for their self-renewal capabilities, cell surface antigens, expression of stemness markers, their ability to differentiate, and to initiate tumor formation (Harford-Wright et al., 2017). Mesenchymal (GSC1 and GSC4) and classical (GSC9) GSCs were maintained as non-adherent spheres in NS34 medium (DMEM-F12 with N2, G5, and B27 supplements, plus Glutamax and antibiotics, Life Technologies). Differentiated glioblastoma cells (DGCs) were generated from GSCs cultured in DMEM/F12 with 10% fetal bovine serum (FBS), Glutamax, and antibiotics (Life Technologies) for at least 10 days. Differentiation was controlled

using morphology, TUBB3 increase in expression, and concomitant SOX2 and NESTIN loss of expression (Figure S1).

Jurkat T-cells were purchased from American Type Culture Collection.

METHOD DETAILS

Glioblastoma xenografts and safety evaluation of NSA

GSC9 was transduced with GFP and luciferase (pLNT-LucF/pFG12-eGFP mixture plasmid, a kind gift of Valérie Trichet, Université de Nantes, France). 10^6 and 10^5 modified patient-derived cells were implanted in Balb/c Nude (BALB/cAnNRj-Foxn1 nu/nu) mice (Janvier Labs), subcutaneously in each flank and orthotopically in the striatum, respectively. Tumor growth was monitored each week by bioluminescence on a Photon IMAGER (Biospace Lab) 10min after injection of D-luciferin (Interchim FP-M1224D).

For xenograft experiments, treatments with vehicle (10% DMSO in PBS) or NSA (5 mg/kg) were commenced five days post-GSC grafts, three times a week, until a critical point was reached or the conclusion of the experiment at day 50. At euthanasia, indicated organs were weighed and frozen; total blood was collected by an intracardiac puncture on EDTA tubes and centrifugated (1000g, 15min, 4°C) before freezing at -80°C . Blood analysis was performed using a Hemavet analyzer (Therassay core facility, Nantes, France). PFA-fixed and OCT embedded brain tissue sections (8 μm , Cryostat, Leica) were stained with Hematoxylin and Eosin using standard protocol (Harford-Wright et al., 2017). Alternatively, cryostat sections were fixed in cold methanol, permeabilized (0.5% Triton-X100), blocked in PBS-BSA 3%, and incubated with antibodies to NESTIN (Millipore MAB5326, 1/300) and ISOLECTIN GS-IB4 (I21413, Life Technologies) overnight at 4°C in 3% BSA.

For safety evaluation of NSA in mice, the compound was injected intraperitoneally (5 mg/kg) in non-tumor-bearing mice three times per week for 4 weeks. The toxicity score of NSA was determined each week depending on weight, body condition, and mouse behavior (grading from 1 for normal to 3 for critical). Liver transaminases ASAT and ALAT were measured at the hospital biology platform (CHU Hotel-Dieu, Nantes, France).

The Cancer Genome Atlas (TCGA) analysis

The Cancer Genome Atlas (TCGA) database was explored via the Gliovis platform (<http://gliovis.bioinfo.cnio.es>; Bowman et al., 2017). We interrogated RNAseq data from glioma patients for the expression of *MLKL* and EV-related genes, as well as for the probability of survival, according to histological glioma status (glioma grades II to IV), glioblastoma subtypes based on Verhaak classification (classical, mesenchymal, neuronal, and proneuronal) (Verhaak et al., 2010) and *IDH1* mutation status.

MLKL targeting

To knock down *MLKL* expression, RNA interference was performed using 10 pmol of duplexes targeting human *MLKL* (GCAACGCAUGCCUGUUUCACCAUA, Stealth siRNA from Life Technologies) or non-silencing control duplexes (low-GC 12935111, Life Technologies) mixed with OptiMEM and Lipofectamine RNAi-MAX Transfection Reagent (Life Technologies). Alternatively, endogenous *MLKL* protein was depleted by taking advantage of the Trim-away TRIM21/proteasome system recently described (Clift et al., 2017,2018). Briefly, *MLKL* antibody (Abcam ab211045, 4 μg) was electroporated in 5×10^5 GSCs with a Neon electroporation system according to the manufacturer's instructions (Life Technologies). Pharmacological targeting of *MLKL* was achieved using *in vitro* treatment with necrosulfonamide NSA (Abcam, ab143839, 5 μM). Combination with temozolomide (TMZ, Sigma PHR1437, 100 μM) was used as indicated.

Immunoblotting

For human tissues, protein lysates from adult normal brains and brain tumors were obtained from GeneTex (GTX28771) and NovusBio (NB820-59423), respectively. For cell culture, lysis was performed, after one cold PBS wash, in TNT buffer (50 mM Tris pH7.4, 150 mM NaCl, 1% Triton X100, 1% Igepal, 2 mM EDTA, supplemented with protease inhibitor cocktail) for 30min on ice. Lysates were clarified at 10000g for 5min. Protein concentration was determined using a MicroBCA protein assay kit (Thermo Scientific). 10 μg of proteins were resolved in Tris-acetate SDS-PAGE and transferred to nitrocellulose membranes (GE Healthcare). For extracellular vesicle fractions, pelleted EVs from an identical number of viable cells were directly lysed

in boiling Laemmli 2X. Membranes were revealed using a chemiluminescent HRP substrate (Millipore) and visualized using the Fusion imaging system (Vilber Lourmat).

Antibodies

The following primary antibodies were used: MLKL (Cell Signaling 14993), GAPDH (Santa Cruz sc-32233), CD9 (System Biosciences EXOAB-CD9A-1), GM130 (Abcam ab52649), Steap3 (Abcam ab151566), RAB14 (Santa Cruz sc-271401), M6PR for WB (Cell Signaling 14364), M6PR for immunofluorescence (Abcam ab2733), CD63 for WB (System Biosciences EXOAB-CD63A-1), CD63 for immunofluorescence (BD Biosciences 556019), SOX2 (Millipore AB5603), NESTIN (Millipore MAB5326), LAMP2 (Santa Cruz sc-18822), phospho-Histone H3 (Cell Signaling 3377), caspase-3 (Cell Signaling 9662), caspase-8 (Cell Signaling 9746), PARP (Santa Cruz sc-8007), GSDME (Abcam ab215191), phospho-ATM (Cell Signaling 5883), phospho-p65 (Cell Signaling 3033), P65 (Santa Cruz sc-372), phospho-I κ B α (Cell Signaling 9246), I κ B α (Cell Signaling 4814), RIPK1 (BD Biosciences 551042), RIPK3 (Bethyl 13526), TUBULIN (Santa Cruz sc-8035), phospho-MLKL S358 (Abcam 187091), ALIX (BioLegend 634502), EEA1 (BD Biosciences 610456), RAB27A (Cell Signaling 95394), cleaved-caspase 3 (Cell Signaling 9664), and eGFP (Millipore AB10145). HRP-conjugated antibodies (1/5000) were from Southern Biotech, and Alexa-conjugated antibodies (1/200) from Life Technologies.

Isolation of extracellular vesicles (EVs)

GSC-derived EVs were isolated from 4 to 5×10^6 GSCs seeded in 10mL NS34 media (a serum-free and exogenous EV-free culture media) for 48h. DGC-derived EVs were isolated from 80% confluent cells in 10mL DMEM/F12 with 10% fetal bovine serum (FBS), glutamax, and antibiotics (Life Technologies) for 48h. The complete media was depleted from EVs with 16h-ultracentrifugation (100000g, 4°C) before incubation with DGCs. Differential ultracentrifugations (dUC, 4°C) were performed to isolate EVs from conditioned media: 300g 3min, 2000g 10min, 10000g 30min (10k fraction), and 100000g 2h (100k fraction) on a Beckman Coulter ultracentrifuge (OPTIMA L-80) using SW-41 Ti rotor. 10k and 100k pellets were washed in 0.22 μ m filtered PBS, ultracentrifuged (100000g, 2h), and resuspended in filtered PBS. OptiPrep top to bottom density gradients 5% to 40% were performed in 12mL open-top polyallomer tubes (Beckman Coulter), as described (Van Deun et al., 2014). 1mL fractions were collected from the top and washed in PBS. To isolate murine circulating EVs, total blood was harvested by intracardiac puncture and plasma separation was performed at 1000g for 15min before freezing at -80°C until further use. 200 μ L of thawed plasmas were serially centrifuged at 2000g (10min), 10000g (30min), and 100000g (2h). Experimental parameters were submitted to the open-source EV-TRACK knowledge base (EV-TRACK.org) (EV-TRACK Consortium et al., 2017), EV-TRACK ID is EV210024.

Quantification of particles

Single-particle tracking was performed by Tunable Resistive Pulse Sensing (TRPS) using qNano gold apparatus (IZON). Diameter and concentration of 100k and 10k EVs were determined using np100 nanopore (detected range 50–330 nm) and np400 (185–1100nm), respectively. Alternatively, the abundance of EVs was determined using the ELISA kit for human CD63-positive particles according to supplier instructions (ExoELISA-ULTRA CD63, System Biosciences). In addition, single-particle tracking was determined using interferometry light microscopy (Videodrop, Myriade) measuring particle concentration in a real-time nanometer-scale optical method.

Cryo-electron microscopy

Cryo-electron microscopy images of EVs were acquired at the Microscopy Rennes Imaging Center (MRic, Université de Rennes 1, Rennes, France) using 200 kV Tecnai G2 T20 Sphera microscope (Thermo Fisher Scientific), equipped with a TemCam XF416 camera (TVIPS) and a single axis cryo-holder model 626 (Gatan Microscopy). Freshly isolated EVs were deposited on glow-discharged electron microscope grids, followed by vitrification by rapid freezing into liquid ethane using an automatic plunge freezer (EM GP, Leica) under controlled humidity and temperature. Neither dehydration nor chemical fixatives were used, allowing observation of the EVs in their native states.

Confocal and super-resolution microscopy

Cells attached to poly-lysine slides were fixed with PBS-PFA 4% and permeabilized with Triton X100 (except for p-MLKL: a PBS-BSA 3%, Triton 1%, and Saponin 1% solution was used for permeabilization and

antibodies incubation). Primary antibodies were incubated overnight in PBS-BSA 4% at 4°C and AlexaFluor-conjugated secondary antibodies for 45min at room temperature. Samples were mounted in Prolong gold anti-fade with DAPI (Life Technologies). Confocal images were acquired on confocal Nikon A1Rsi (Nikon Excellence Center, MicroPiCell facility, Nantes, France). Super-resolution microscopy using structure illumination microscopy (SIM) images were acquired with a Nikon N-SIM (Nikon Excellence Center, MicroPiCell facility, Nantes, France) using a 100× oil-immersion lens with a 1.49 aperture and reconstructed in 3D using the NIS-Element Software. All images were analyzed using the Fiji software.

Proteomic analysis of EVs

Mass spectrometry was done in collaboration with the 3P5 Proteom'IC facility (Université de Paris, Institut Cochin, Paris, France). Peptide contents from 100k EV fractions were lysed and denatured in SDS 4%, 50mM Tris pH = 8 (5min at 95°C). Disulfide bridges were reduced (TCEP 20 mM) and subsequent free thiol groups were protected using chloroacetamide 50 mM. Proteins were digested overnight with trypsin and prepared with S-trap (<https://www.protifi.com/s-trap/>). Nano Liquid Chromatography with Tandem Mass Spectrometry analysis (nLC-MS/MS) was then performed, and peptides were concentrated, separated, and analyzed with an Ultimate 3000 Rapid Separation liquid chromatographic system coupled to a Q-exactive mass spectrometer (Thermo Fisher Scientific). Raw data were processed with MaxQuant software to perform a comparison of experimental MS/MS peptides fragmentation data with the *Homo sapiens* taxon of the Swiss-Prot Uniprot database. Identified proteins were processed through the STRING online database (<https://string-db.org>).

Transcriptomic analysis

Cells were lysed and RNA content was analyzed by 3' Sequencing RNA Profiling at the Genomics and Bioinformatics Core Facility (GenoBiRD, Biogenouest, IFB, Nantes). Briefly, total RNA was isolated using the RNeasy Mini Kit (Qiagen) and clean samples (DO 260/280 and 260/230 > 1.8) were submitted for quality control on a Bioanalyzer Tape Station (Agilent). RNA libraries were prepared and HiSeq sequencing was carried out (HiSeq 2500, Illumina). Data were demultiplexed and analyzed with Illumina Bcl2fastQ2 software. Reads were aligned against human reference transcriptome (hg19) and differential analysis was performed with DESeq2 tool and annotated with Gene Ontology and Kegg pathways (methods available on <https://bio.tools/3SRP>).

Stemness assays

To analyze the self-renewal properties of GSCs, tumorsphere formation and extreme limiting dilution assay (ELDA) were performed. For tumorsphere formation, GSCs (100/μL) were seeded in triplicate in NS34 media. Cells were dissociated manually on both the second and third days to reduce cell aggregation influence. On day 5, the number of tumorspheres per field of view (NS/fov) was calculated by single-blinded counting 5 random fov per condition. To analyze further self-renewal of GSCs, ELDA was performed as reported (Harford-Wright et al., 2017; Jacobs et al., 2020). Briefly, GSCs were plated in a 96-well plate using serial dilution ranging from 2000 to 1 cell per well (one column, i.e. 8 replicates per dilution) and treated or not with NSA. After 14 days of cell culture, each well was binarily evaluated for the presence or the absence of tumorsphere in single-blind count. Stemness frequency was then calculated using online ELDA software (<http://bioinf.wehi.edu.au/software/elda>; Hu and Smyth, 2009). The mean stemness frequency was calculated by averaging 3 independent experiments.

Proliferation and cytotoxicity assays

GSC viability was assessed using Uptiblu (UP669413, Interchim) and CellTiter-Glo (G9243, Promega) following manufacturers' protocols. Absorbance and luminescence were measured on a FluoStar Optima (BMG Labtech) plate reader and the percentage of cell viability was determined in comparison to control/vehicle conditions. For EdU proliferation analysis, cells were incubated with EdU (10 μM, 2h), followed by fixation and Click-it reaction according to instructions for flow cytometry (Life Technologies, C10424) or by secondary antibody incubation for confocal analysis (Life Technologies, C10337). Propidium Iodide (PI) and Annexin V staining (Life Technologies, V13245) were used to assess cell death induction following treatment according to the manufacturer's instructions.

Flow cytometry

Flow Cytometry analyses were performed on FACSCalibur (BD Biosciences, CytoCell facility, Nantes, France) and processed using FlowJo software (BD Biosciences).

Chemicals

Necroptosis was induced *in vitro* by pre-treatment 30min with Q-VD-OPh (R&D Systems, 10 μ M) and Birinapant (Selleckchem, 5 μ M) prior stimulation with TNF α (R&D Systems, 10 ng.mL⁻¹) for 48h. Necroptosis was blocked using Necrostatin Nec (Selleckchem, 20 μ M).

RT-PCR and-qPCR

RNA extraction was done using Qiagen RNeasy kit and equal amounts of RNA were reverse transcribed using the Maxima Reverse Transcriptase kit (ThermoFisher). PCR was performed on the resulting cDNA using Red Taq DNA polymerase (Sigma). Semiquantitative qPCR was performed using PerfeCTa SYBR Green SuperMix (QuantaBio). The following primers were used for human targets: MLKL forward GCCACTGGAGA TATCCCGTT, MLKL reverse CTTCTCCCAGCTTCTGTCC, SOX2 forward CAAAAATGGCCATGCAGGTT, SOX2 reverse AGTTGGGATCGAACAAAAGCTATT, TUBB3 forward CAGATGTTGATGCCAAGAA, TUBB3 reverse GGGATCCACTCCACGAAGTA, RIPK1 forward AGTGACTTCCTGGAGAGTGC, RIPK1 reverse TCATCATCTTCGCCTCCTCC, RIPK3 forward CTCTCTGCGAAAGGACCAAG, RIPK3 reverse TCGTAGCCCCACTTCCTATG, RAB27B forward CTTGCGAGGCTGACCGA, RAB27B reverse CCACA CACTGTTCCATTTCGC, ACTB forward GGAATTCGAGCAAGAGATGG, ACTB reverse AGCACTGT GTTGGCGTACAG, HPRT1 forward TGACACTGGCAAAACAATGCA, HPRT1 reverse GGTCTTTTCAC CAGCAAGCT. Data were analyzed by the 2- $\Delta\Delta$ Ct methods and normalized using the two housekeeping genes ACTB and HPRT1.

siRNA

RNA interference targeting human *RAB27A* and *RAB27B* was performed as previously described (Douanne et al., 2019).

Phos-tag

Commercial Phos-tag SDS-PAGE gels were purchased from FUJIFILM Wako Pure Chemical corporation to assess basal MLKL phosphorylation in GSCs. Briefly, 1.10⁵ GSCs were washed and lysed directly in 30 μ L Laemmli (10min, 95°C). 1 mM of ZnCl₂ was added to the samples prior to running on 12.5% Phos-tag gels. Gels were washed in transfer buffer (Biorad) containing 10mM EDTA and 0.5% SDS before transfer to nitrocellulose membranes for immunoblotting analysis.

Uptake and co-culture with EVs

PKH-67 (Sigma) staining of EVs was performed as previously described (Treppe et al., 2016). 5.10⁵ GSCs were seeded in 1mL of NS34 with the labeled EVs for 4h. After 10min fixation in PBS-PFA 4% and washes, flow cytometry analyses were performed on a FACSCalibur (BD Biosciences, CytoCell facility, Nantes) and processed using FlowJo software. Alternatively, EVs isolated from 5.10⁶ GSC9 control (ctrl) or MLKL-targeted (NSA and siMLKL) called EV_{ctrl}, EV_{vehicle/NSA} and EV_{siMLKL} were added daily to GSC9, either naïve or pre-incubated with either siMLKL and sic, or NSA and vehicle, at a dose of ten producing cells for 1 receiving cell (10:1) or one for one (1:1), as described in Figures S6B and S6C. Viability using Uptiblue was assessed after 48h.

IncuCyte

Effect of NSA treatment was recorded in real-time on live cells using IncuCyte Zoom live cell imaging system (Essen BioScience). Briefly, GSCs were seeded at a density of 5000/well in a 96-well plate, treated with NSA (Abcam, 5 μ M) or vehicle, and maintained at 37°C and 5% CO₂ during the time of the experiment. Phase contrast images (10X zoom) were taken every 2h for 4 days.

Electron microscopy

Electron microscopy images of EVs were acquired thanks to Joëlle Veziers (SC3M core-facility, CHU Nantes, France). Isolated EVs were fixed in glutaraldehyde 1.6%, diluted in 0.1M phosphate buffer, pH = 7.2, coated on formvar carbon copper grids (AgarScientific), stained with Uranylless (Delta Microscopies),

and observed with a Jeol JEM-1010 transmission electron microscope. For electron microscopy, cells were fixed in 2.5% glutaraldehyde/2.0% paraformaldehyde, diluted in 0.1M Cacodylate buffer, at 4°C overnight. Samples were then stained in 0.05% Green malachite/2.5% glutaraldehyde and post-fixed with 1% OsO₄ and 0.8% K₄Fe(CN)₆ for 45min on ice. Samples were stained with 1% Tannic acid for 20min on ice and with 1% uranyl acetate, overnight at 4°C. Samples were stepwise dehydrated in Ethanol and embedded in Epon. 100nm thin sections were collected in copper mesh grids, contrasted with 1% uranyl acetate followed with 0.4% lead citrate (Sigma-Aldrich), and imaged with a Hitachi 7500 transmission electron microscope equipped with Hamamatsu camera C4742-51-12NR.

Secretory pathway assay

Gaussia luciferase plasmid (Addgene #22522) was transfected in GSCs using the Neon system (Life Technologies). 8000 transfected cells were plated in a 96-well plate 24h later and treated as indicated. Supernatants were then collected and analyzed for Gaussia luciferase activity using the Pierce Gaussia Luciferase Glow assay kit following manufacturers' protocol (Thermo Scientific, 16160).

QUANTIFICATION AND STATISTICAL ANALYSIS

Data are expressed as mean \pm s.e.m. and are representative of at least three independent experiments unless otherwise stated. Statistical analysis was performed with GraphPad Prism8 using two-way ANOVA, parametric t-test, or non-parametric Mann-Whitney when required. For each statistical test, a p-value <0.05 was considered significant.